How do Cells Decide Where to Go

by

Jupiter Algorta

B.Sc., The University of British Columbia, 2023

A THESIS SUBMITTED IN PARTIAL FULFILLMENT OF
THE REQUIREMENTS FOR THE DEGREE OF

MASTER OF SCIENCE

in

The Faculty of Graduate and Postdoctoral Studies

(Mathematics)

THE UNIVERSITY OF BRITISH COLUMBIA

(Vancouver)

August 2025

The following individuals certify that they have read, and recommend to the Faculty of Graduate and Postdoctoral Studies for acceptance, the thesis entitled: **How do Cells Decide Where to Go**

submitted by **Jupiter Algorta** in partial fulfillment of the requirements for the degree of **Master of Science** in **Mathematics**.

Examining Committee:

Leah Edelstein-Keshet, Professor, Department of Mathematics, UBC
Supervisor

Anotida Madzvamuse, Professor, Department of Mathematics, UBC
Supervisory Committee Member

Jimmy Feng, Professor, Department of Mathematics, UBC
Supervisory Committee Member

Abstract

To find sites of infection, neutrophil cells, the immune system's first responders, must polarize, establishing a clear front and back, to enable directed migration. This polarization is regulated by the GTPase protein Rac. One minimal model by Mori et al. (2018) captures this polarizing behaviour using a reaction–diffusion (RD) system, namely the "Wave-Pinning" (WP) model. A recent publication by Town and Weiner (2023) tracked Rac activity in neutrophil-like migratory cells, recording both temporal and spatial profiles of Rac as well as the resulting cell trajectories under different stimulation protocols. In collaboration with Orion Weiner's lab (UCSF), I evaluated variants of the WP model against experimental datasets. Town and Weiner hypothesized the existence of a local Rac inhibitor downstream of active Rac. I extend the WP framework by introducing this feedback loop and test whether it can explain the observed data. To simulate migratory cells while solving the RD system inside the cell, I used the Cellular Potts Model (CPM), with partial differential equations solved along the 1D cell edge. To simulate cell shape and migration, I used the CPM (implemented in open-source software, Morpheus) to capture cell morphodynamics, with the RD system solved along the cell edge; high Rac was assumed to promote edge protrusion. I show that the hypothesized local Rac inhibitor enables the model to reproduce both qualitative and quantitative experimental results, including key cell trajectories. The inhibitor also enhances the cell's ability to track stimuli. However, to account for other observed behaviours, I showed that an upstream intermediate (PIP3) plays an important role. Together, the WP-Inhibitor-PIP3 model suffices to explain the dataset, providing a minimal mechanistic model of Rac regulation consistent with experimental observations.

Lay Summary

Immune cells move towards infections and injuries by forming a "front" and "back", protruding at the front and contracting at the back. This internal polarization is guided by chemical signals and internal feedback loops. Recent experiments revealed a new, local negative feedback that helps cells respond more flexibly. In this thesis, I established a collaboration with Orion Weiner's lab at UCSF, through which I extended a model from literature to include this new feedback and used computer simulations to test how it affects cell behaviour. The results show that this added feedback allows cells to better detect and respond to changing or noisy signals.

Preface

The research presented in this thesis is based on the manuscript with the pre-print available in *bioRxiv*:

- Jupiter Algorta, Jason P. Town, Orion D. Weiner, Leah Edelstein-Keshet. "Investigating local negative feedback of Rac activity by mathematical models and cell motility simulations," 2025 [1].

As the primary researcher and lead author of this manuscript, I performed all the computational work and the majority of the analysis. Professors Leah Edelstein-Keshet and Orion D. Weiner, as well as Dr. Jason P. Town, guided me in addressing mathematically and biologically relevant questions, and reviewed and edited the manuscript. Dr. Jason P. Town and Professor Orion D. Weiner have done experiments that provided the data used here to guide my modelling. This was done previously to my work and published in [47].

I used generative AI (ChatGPT 4o / o3) to identify relevant coding packages and to interpret some compilation errors. I reviewed and edited the code as needed.

Table of Contents

Appendix

List of Tables

List of Figures

Acknowledgements

Firstly, I would like to express my immense gratitude to my supervisor, mentor, and friend, Professor Leah Edelstein-Keshet, for giving me the opportunity to join the academic world and for guiding me to achieve heights I otherwise would not have thought possible. Her mentorship throughout this project was invaluable, and this training has paved the road ahead for me. Secondly, I would like to thank my collaborators, Dr. Jason P. Town and Professor Orion D. Weiner, for not only providing an extensive library of data on single migratory cells, but also for the recurring meetings that helped me shape my work and identify the most impactful biological questions to address. Their input allowed me to develop this project mathematically while ensuring that my results remained biologically relevant.

Dedication

To my beloved wife, Abbey, whose love and belief in me have been my comfort through every long day and late night.

To my parents, Martin and Priscila, who supported my dream of becoming an academic and provided the resources for me to achieve it.

And to my younger self, Miguel, who despite all the unfortunate events life brought, held strong with the hope that things would get better, and they did.

Chapter 1

Introduction

1.1 Motivation

Imagine you were placed in a dense forest at night while blindfolded, the only way for you to find your way out being the slight shift of breezes. This may seem like an extreme scenario, but our immune cells go through a similar environment to detect sites of injury or infection. Among the first cells to arrive at the affected site we find the main focus of my research: neutrophil cells [21, 33]. These cells are crucial in the early stages of your immune defence, and they only guide themselves by being able to follow shallow and noisy gradients of an attractive chemical (chemoattractant) [19]. This process is known as chemotaxis, and it is governed by a series of biochemical networks and signals that are triggered by the chemoattractant.

For a neutrophil to migrate, it must exert different forces in various regions of the cell, requiring the biochemical networks to undergo polarization and establish a clear front and back. At the rear, the cell contracts, pulling the membrane inward, while at the front, it pushes the membrane outward, creating protrusions [7]. In my research, I investigated the essential components needed in a model to account for experimental results. I approached this by expanding existing reaction-diffusion models, fitting them to an extensive source of experimental data, and testing hypotheses using a virtual model of the cell in a dish.

1.2 Biology Overview

Cell protrusions are essential for enabling cells to migrate in a directed manner. These protrusions are driven by the polymerization of actin filaments, which are thin, elastic rods that push the cell membrane outward as they grow. This process is regulated by a network of signalling molecules centred around the small GTPase **Rac**, which exists in both active and inactive forms. In its inactive state, Rac diffuses freely within the cell and does not interact with other molecules. When inactive Rac is recruited to the cell

membrane it becomes active. Activation of Rac promotes actin polymerization.

Once an external stimulus reaches the cell's membrane, it binds to cell-surface receptors (specific proteins that activate other effectors inside the cell). Ultimately, this cascade of effects activates Rac. This activation is facilitated by guanine nucleotide exchange factors (GEFs), which promote the exchange of GDP for GTP, while inactivation is promoted by GTPase-activating proteins (GAPs), which enhance GTP hydrolysis [14, 37].

To study this network, our collaborators Dr. Jason P. Town and Professor Orion D. Weiner [47] modified neutrophil-like cells to express light-sensitive receptors, a technique known as **optogenetics** [12].In these cells, Rac could not be directly activated. Instead, illumination triggered recruitment of PI3K [18, 46], a kinase that produces the lipid PIP3 at the membrane. Previous studies [8, 11, 20] have demonstrated that PIP3 enhances Rac activation, so by controlling PI3K with light, Town and Weiner could indirectly and precisely stimulate Rac.

Town and Weiner also introduced biosensor proteins for PIP3 and active Rac, allowing spatial and temporal monitoring through fluorescence microscopy. Because the biosensors emitted at different wavelengths, PIP3 and Rac signals could be distinguished in the same cell.

With this setup, Town and Weiner recorded cell trajectories, stimulation patterns, and biosensor responses, providing the experimental data for my modelling.

1.3 Experimental Protocols

To motivate the following section, I will go through some of the results of Town and Weiner in [47]. With the ability to activate Rac via the PI3K signalling, Town and Weiner were able to perform two types of stimulation protocols, **local** and **global**.

These protocols (local and global, respectively) are shown in panels **(A)** and **(B)** of Figure 1.1. In brief, when the entire cell is illuminated (**global** in the sense of whole-cell illumination, not the mathematical term), this removes any spatial biases from the stimulus. When only part of the cell is illuminated (**local**, meaning illumination on portion of the cell), the stimulus introduces spatial bias and can steer motion.

Using these two types of stimulation Town and Weiner combined them in more complex protocols to study spatial and temporal responses of Rac in both motile and non-motile cells. These different combinations are high-

lighted in panels **(C)** and **(D)** of Figure 1.1.

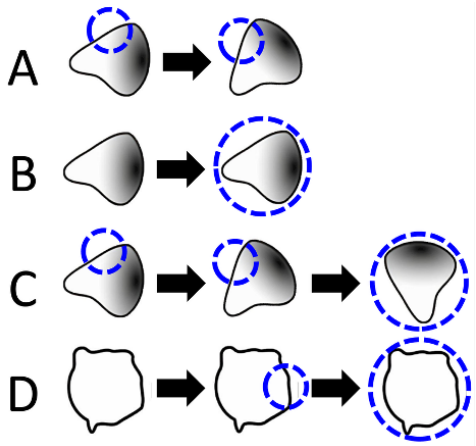

Figure 1.1: The original stimuli in Town and Weiner [47] included some combination of the above protocols in both migratory cells (A-C) and non-motile cells (D). Arrows indicate flow of time. (A) Local stimulus on the side (or front or rear) of a polarized cell (B) Global stimulus of a polarized cell. (C) Local followed by a global stimulus of a polarized cell. (D) Treatment of a cell with latrunculin (to disassemble F-actin) followed by local and then global optogenetic stimulus.

1.4 Experimental Data Overview

Town and Weiner collected both temporal and spatial data on Rac activity using optogenetic stimulation and fluorescent biosensors [47]. To isolate temporal dynamics from movement, Town and Weiner treated cells with latrunculin (Lat) to prevent actin polymerization and immobilize the cell. These non-motile cells were then subjected to global light stimulation, and Rac activity was measured over time across the whole cell. Town and Weiner repeated this in hundreds of cell samples under various global stimulation protocols, including 425 cells across multiple variants of a specific protocol (double-pulse, described in Section 2.2). This yielded a variety of results, as each cell responded slightly differently. Figures will show this average Rac as well as a ± 1 SD (standard deviation) range to show the variation in responses. This variability in responses and the unique behaviour of each cell is referred to as cell heterogeneity. This allowed for the analysis of

activation and adaptation patterns in response to repeated stimuli.

In a separate set of experiments, Town and Weiner studied Rac dynamics in motile cells under spatially local stimulation. By illuminating specific regions of the cell membrane, Town and Weiner could observe how spatially patterned input affects cell movement and polarity. These experiments generated a dataset of cell trajectories and biosensor signals under various stimulation protocols, offering insight into the interplay between Rac activation and cell behaviour.

1.5 Morpheus: Cellular Potts Model

To simulate Rac dynamics at the cell edge within a moving cell, I use the Cellular Potts Model (CPM) implemented via Morpheus [45], a software that supports CPM simulations through an intuitive graphical user interface. In the CPM, the domain is represented as a lattice, where cells are closed subsets and unoccupied sites represent the surrounding medium. Each lattice site is assigned an identity indicating which cell or medium it belongs to. Energy values are assigned to reflect constraints such as target cell area and perimeter, and a Hamiltonian is computed to measure the total energy of the lattice configuration. This Hamiltonian governs the dynamics of the CPM, and updates occur as follows:

- Randomly select a lattice site i
- Choose a random neighbouring lattice site j
- Copy the identity of i into j
- Compute the Hamiltonian of the new configuration
- If the total energy has decreased, accept the new configuration. Otherwise, compute the energy increase (ΔH) and accept the new configuration with probability $e^{-\frac{\Delta H}{T}}$, where T is a temperature parameter that defines the likelihood of accepting higher-energy configurations.

To reduce unnecessary computations, Morpheus includes an option to optimize this update scheme by selecting only lattice sites and neighbours that would result in a change, avoiding redundant updates where a site copies its identity to another site with the same value.

Beyond CPM dynamics, Morpheus enables the solution of reaction-diffusion models in a one-dimensional periodic domain mapped to the cell's edge,

which makes it possible to simulate Rac dynamics at the cell's edge. Note that the PDE is solved in a stationary domain, then mapped to the CPM. Active Rac can also be incorporated into the Hamiltonian to favour cell protrusions in regions where its concentration is high. By integrating the PDE into the moving cell framework, I have replicated experimental results and established a straightforward link between stimulus protocol descriptions and their PDE representations.

1.6 Mathematics Overview

Reaction-diffusion models are commonly used to describe molecules like Rac, modelling their interactions and concentrations [3, 4, 15, 28, 49]. My starting point is the Wave-Pinning (WP) model [32], a reaction-diffusion system that, with the right set of parameters, supports both spatially polarized steady states (which can be used to define the front and back of a cell) and spatially homogeneous solutions [17]. The full PDE model of WP is given as follows:

$$\frac{\partial u}{\partial t} = v\left(k_0 + \gamma \frac{u^n}{K^n + u^n}\right) - \delta u + D_u \nabla^2 u, \tag{1.1a}$$

$$\frac{\partial v}{\partial t} = -v\left(k_0 + \gamma \frac{u^n}{K^n + u^n}\right) + \delta u + D_v \nabla^2 v. \tag{1.1b}$$

This equation models the dynamics of active Rac u, inactive Rac v, with a basal rate of activation k_0 and a nonlinear autocatalytic feedback term of strength γ, shaped by the Hill function with coefficient n and half-maximal activation threshold K. Rac is inactivated at a rate δ. This is summarized in the panel **(A)** of Figure 1.2.

The diffusion rate of active Rac is much lower than that of the inactive form. This is motivated by the biological context in which active Rac is bound to the membrane. One important feature of the model is that, in periodic or Neumann boundaries, the total mass of Rac over all space (Ω) is held constant:

$$\int_\Omega (u + v) d\Omega = T. \tag{1.2}$$

Here I will only work in 1D periodic domains, that would be representing the cell's edge when looking at the 2D cell images. Thus, the cell's "front" is defined as the region with the highest concentration of active Rac which is shown in panel **(B)** of Figure 1.2

My initial extension of the WP model added a spatio-temporal parameter to describe how the light stimulus contributes to the rate of Rac activation.

As previously noted, Morpheus allows me to implement the distribution of Rac, its effector(s) and/or upstream signals along a 1D periodic stationary domain to the cell edge. The distribution of active Rac is linked to edge protrusion and hence dictates the cell's direction of motion (Figure 1.2, C).

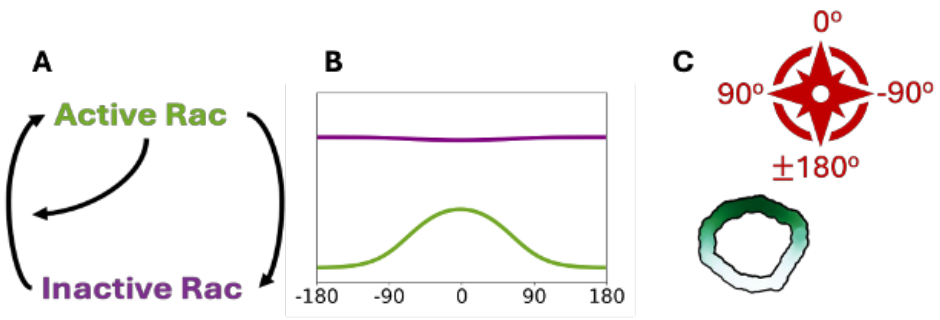

Figure 1.2: (A) Basic set of interactions in the simplest model for Rac by Mori et al [32] ("wave-pinning") is formulated as a set of reaction-diffusion PDEs shown in Equation (1.1). (B) The model predicts the distribution of active (green) and inactive (purple) Rac along the cell edge, (a periodic 1D stationary domain on the cell edge, shown unwrapped in panel B). (C) A polarized cell is represented by the same nonuniform Rac activity distribution along its edge, with high Rac (dark green) defining the cell front. (Here the cell is polarized Northward, i.e., active Rac zone peaks at 0°.) The shape of the cell and its trajectory is simulated in the software Morpheus. The "compass" indicates the lab frame of reference, with 0° corresponding to the northwards direction. In simulations, the cell edge is shown as a wide band for easier visualization of the Rac distribution.

To model the optogenetic control I introduce a spatio-temporal quantity, $0 \leq S(x,t) \leq 1$ that represents the intensity, localization, and timing of the optogenetic stimulus. Assuming that the stimulus enhances Rac activation, I define a constant parameter α to convert stimulus intensity to the rate of Rac activation.

$$\frac{\partial u}{\partial t} = v\left(k_0 + \alpha S(x,t) + \gamma \frac{u^n}{K^n + u^n}\right) - \delta u + D_u \nabla^2 u, \tag{1.3a}$$

$$\frac{\partial v}{\partial t} = -v\left(k_0 + \alpha S(x,t) + \gamma \frac{u^n}{K^n + u^n}\right) + \delta u + D_v \nabla^2 v. \tag{1.3b}$$

This allows me to simulate their local and global stimulation patterns, as shown in Figure 1.3.

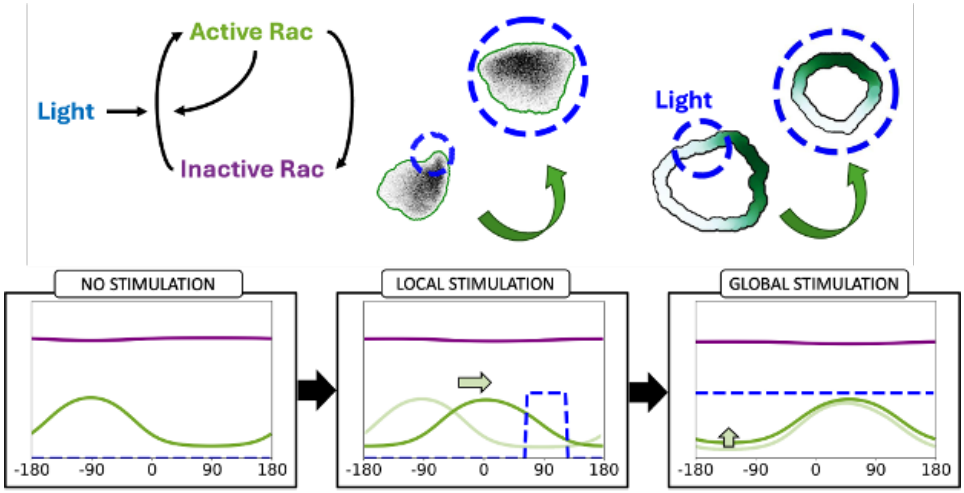

Figure 1.3: The light stimulus is assumed to increase the rate of Rac activation in the models. The location of the stimulus is represented by the dashed circle (top). We track the location of the stimulus and the model components in the 1D profile (bottom row) as well as the moving cell edge simulation. Blue: light stimulus, green: active Rac concentration, purple: inactive Rac concentration along the cell perimeter.

I first tested the simple WP model of Mori et al [32] and its predictions for the polarity and motion of a cell exposed to basic local optogenetic protocols shown in Figure 1.4. Note that in experiments (labelled "Experiments" in Figure 1.4) the local stimulus at the rear of a polarized cell will cause the cell to reorient and make a U-turn, while two local stimuli at opposite sides of the cell will result in one or another direction (right or left) "winning", and cause the cell to turn right or left. We found that the WP model, with the optogenetic control, easily accounts for such behaviour.

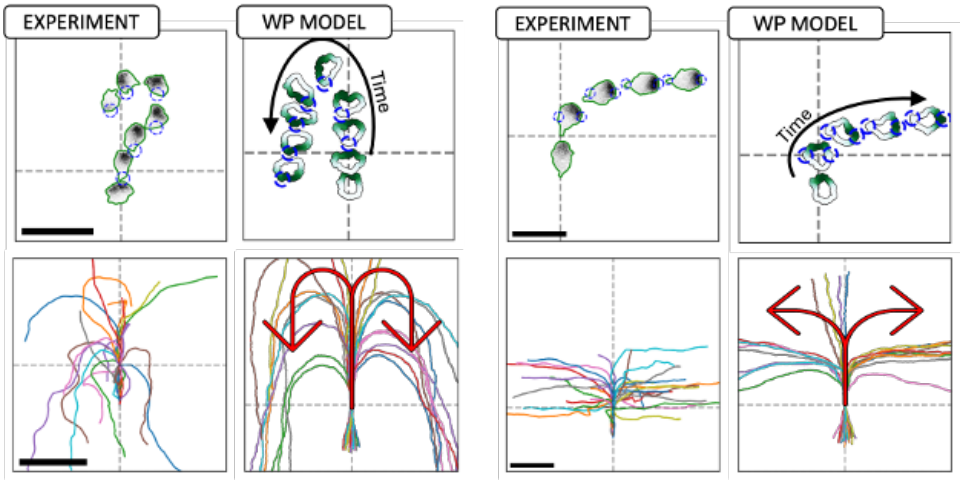

Figure 1.4: The simplest model for Rac (WP with optogenetic control, Equation (1.3)) can satisfactorily account for cell motility responses to basic local optogenetic stimuli. Left two columns: experimental data and model predictions for local rear stimulation; the cells make U-turns and move in the reverse direction. Right two columns: competing two-sided local stimuli; The cell selects one or the other side and turns. Scale bar: 50µm. This demonstrates that, qualitatively, the WP model can reproduce the observed experimental cell behaviour for basic stimuli. The dashed axis indicates where the stimulation started.

1.7 Stationary Domains and Migratory Cells

Although all models in this thesis are solved on stationary domains, they can be mapped to the cell boundary in a CPM framework using Morpheus [45]. This mapping allows the Rac dynamics to be interpreted directly along the evolving edge of a simulated cell. Importantly, the underlying equations are still solved on a fixed domain, the CPM implementation simply provides a way to visualize and test how these stationary-domain models would behave in migratory cells.

1.8 Inhibitor Hypothesis

With the setup described, Town and Weiner recorded cell trajectories, stimulation patterns, and biosensor responses. Two particularly informative ex-

periments are shown in Figure 1.5, where Town and Weiner combined their stimulation protocols with measurements of Rac activity in both non-motile and motile cells.

In the first column of Figure 1.5, results for non-motile cells are shown. A global stimulation is applied on the cell and the average Rac activity across the entire cell is recorded over time, normalized by the pre-stimulation average activity level. Both graphs show experiments where the whole cell was illuminated for 180 seconds, followed by a resting period, and then illuminated again for another 180 seconds. The top shows a 120-second rest, the bottom a 60-second rest.

What is noticeable is that when the cell is stimulated, Rac is rapidly activated, achieving a peak, which is followed by a decay even with persistent stimulation. Another feature is that in the second stimulation, the peak is smaller than the first, especially with shorter resting times. These results led Town and Weiner to hypothesize the existence of a delayed Rac inhibitor, something that could explain a rapid activation followed by a decay, and a diminished response upon repeated stimulation.

In the motile cell experiment, shown in the middle and right columns of Figure 1.5, a more complex stimulation protocol was used. Initially, cells were stimulated on their "left side," 90° counterclockwise from their direction of motion. This local stimulation guided the cells to rotate counterclockwise. After some time, a global stimulus was applied to the same cells. Town and Weiner proposed three mutually exclusive outcomes, each leading to a different hypothesis: (1) Cells would persist on their counterclockwise rotation, indicating a running advantage. (2) Cells would go in a straight path, being history-independent with what happened previously. (3) Cells would rotate clockwise, which would be a novelty result. What Town and Weiner found is that, with statistical significance, cells would rotate clockwise, namely (3). This surprising result further supported the idea of a delayed inhibitory component acting downstream of Rac.

To define the topology of the network, including this proposed inhibitor, Town and Weiner treated non-motile cells with a small molecule named EHT1864, which has been shown to inhibit the downstream effects of active Rac [44]. With higher concentrations of EHT1864, the Rac response over time was closer to a step function. This indicates that Rac activity is needed for its inhibitor, forming a negative feedback loop. Results from this experiment are shown in Figure 1.6.

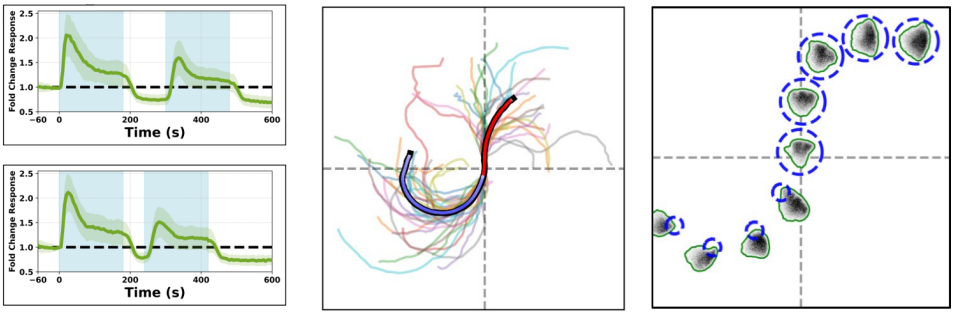

Figure 1.5: Distinct types of experimental data used as inputs or validation for my in my modelling. **(Left column:)** Experimental data of the mean active Rac (solid green curves) ±1 SD (green shading). Light blue represents stimulus ON phase. Top: a longer delay ($\Delta t_1 = 120s$). Bottom: a shorter delay ($\Delta t_2 = 60s$).**(Middle and right columns):** Cells stimulated by local optogenetic inputs followed by global stimulation first turn in one direction, then reverse. Experimental data show the directional behaviour and trajectories of cells, with tracked positions (middle column) and snapshots (right column). Tracks are displayed with the average trajectory overlaid and colour-coded by rotation direction: blue for counterclockwise (CCW), red for clockwise (CW). Figures adapted from [47] with the authors' permission.

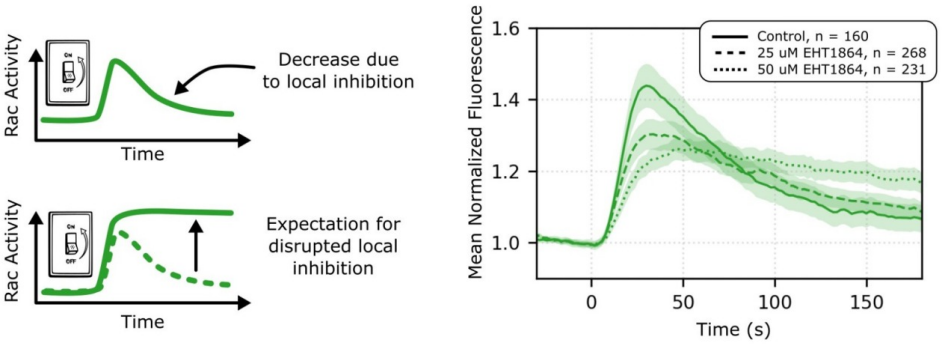

Figure 1.6: Green curves show Rac activity over time, with 95% CI shaded. EHT1864 is a small molecule that inhibits the downstream effects of Rac activity. The correlation between the concentration of EHT1864 and the disruption of the Rac activity suggests a negative feedback loop. Figure from [47] with the authors (Town and Weiner) permission. This figure is licensed under CC BY 4.0.

In this thesis I will show my investigation of this proposed inhibitor, to assess Town and Weiner's hypothesis that the inhibitor alone can account for the data. The networks I explored are shown in Figure 1.7, and their equation and results will be discussed in the following chapters.

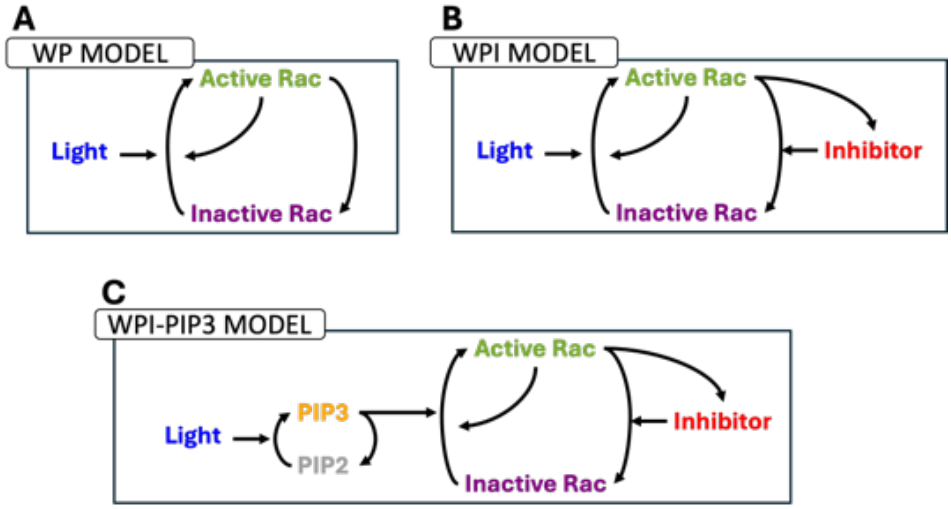

Figure 1.7: **(A)** The simplest model for Rac activation follows the Wave-Pinning (WP) polarity model of Mori et al [32] plus optogenetic control. **(B)** A Rac-associated inhibitor, proposed by Town and Weiner [47] is included in the WPI (Wave-Pinning with Inhibitor) model. **(C)** The role of PIP3 was also considered in the WPI-PIP3 model. A model with PIP3 and no inhibitor was tested and results are shown in the Section 5.3.

Chapter 2

Temporal Dynamics

As described in Section 1.4, Town and Weiner immobilized cells with latrunculin (Lat) to abrogate filamentous actin and measured average Rac levels over time under global stimulation, without spatial variation. Town and Weiner repeated this across hundreds of cells, yielding heterogeneous responses, figures will show the average Rac with a ± 1 SD range. This allowed me to fit not only the mean response but also to generate a distribution of parameters that captures this heterogeneity (fitting algorithm in Section 2.4). The time-dependent levels of PIP3 and active Rac were quantified by Town and Weiner [47]. This temporal data provides an opportunity to work with a simplified ODE version of the WP model (Equation (1.3)). To do so, I omit the diffusion terms, resulting in an ODE that describes the reaction terms of active and inactive Rac. In the ODE case the integral in Equation (1.2) becomes simply

$$u + v = T, \tag{2.1}$$

over time. This allows for a further simplification by replacing v with $(T-u)$ so the model for active Rac (u) becomes:

$$\frac{du}{dt} = (T-u)\left(k_0 + \alpha S(t) + \gamma \frac{u^n}{K^n + u^n}\right) - \delta u. \tag{2.2}$$

Recall that in Equation (1.3) I had defined $S(x,t)$ as a spatio-temporal quantities to mimic optogenetic control. Since the temporal data is for non-motile cells under global stimulation (spatially homogeneous input) this can be changed to be simply $S(t)$ taking values between 0 and 1 and scaled by the paramter α.

Now to consider the inhibitor, a new variable h is introduced as the inhibitor, which promotes Rac inactivation at rate k_1, is promoted by active Rac at rate k_h, and decays at rate δ_h. These additions form the Wave-Pinning with Inhibitor (WPI) model:

$$\begin{aligned} \frac{du}{dt} &= (T-u)\left(k_0 + \alpha S(t) + \gamma \frac{u^n}{K^n + u^n}\right) - (\delta + k_1 h)u, \\ \frac{dh}{dt} &= k_h u - \delta_h h. \end{aligned} \tag{2.3}$$

2.1 Single-Pulse Stimulus

First, cells were exposed to a light stimulus that was turned "ON" instantaneously. The data displays features of adaptation [5], including a rise in active Rac response, followed by decay back to its basal level. In Figure 2.1 experimental observations (left), as well as model fits (fitting algorithm discussed in later sections) for WP (centre) and WPI (right) are shown. The WPI model better captures Rac dynamics than WP. Its delayed inhibitor allows for a rapid Rac response followed by decay, explaining the observed overshoot. In contrast, WP lacks this feedback, so Rac activity remains high during stimulation.

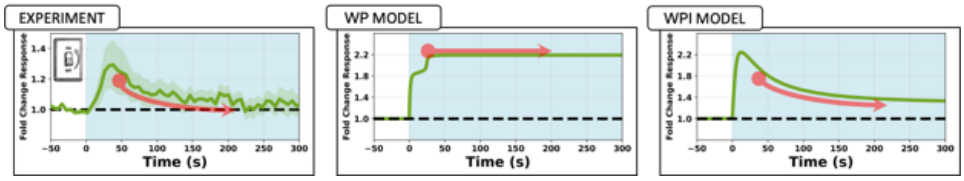

Figure 2.1: Active Rac fold change responses in green. Left: experimental data for an "ON" switch pulse stimulation of latrunculin-treated cells. Centre: WP model predictions. Right: WPI model predictions. WPI is better at fitting the data and accounting for the decay following peak Rac activity. PIP3 levels quantified in the experiments were used as a direct input to Rac (as surrogate for the light stimulus) for the WP and WPI model.

2.2 Double-Pulse Stimuli

A second type of stimulus used on Lat-treated cells was a double-pulse, consisting of two ON-OFF step functions, either $\Delta t_1 = 120s$ or $\Delta t_2 = 60s$ apart (top and bottom rows, respectively, in Figure 2.2). I compare the experimental data (left panels) in Figure 2.2 to model predictions. It is typically observed that the second peak of Rac activation is smaller than the first peak, and significantly smaller if the pulses occur in rapid succession.

The WP and WPI models were fitted as before, with PIP3 data used as a surrogate for the stimulus to Rac. The parameters found from the fitting procedure were used to solve the WP and WPI models and resulted in predictions shown in the centre and right columns of Figure 2.2. The WPI (but not the WP) model was able to account for several features of the experimental observations, namely the relative height of the first and second peaks ($\Delta H_1, \Delta H_2$, see right panels), and the "undershoot" of Rac activity (which fell below its unstimulated level) between and after the stimuli. The WP model failed to reproduce these observations.

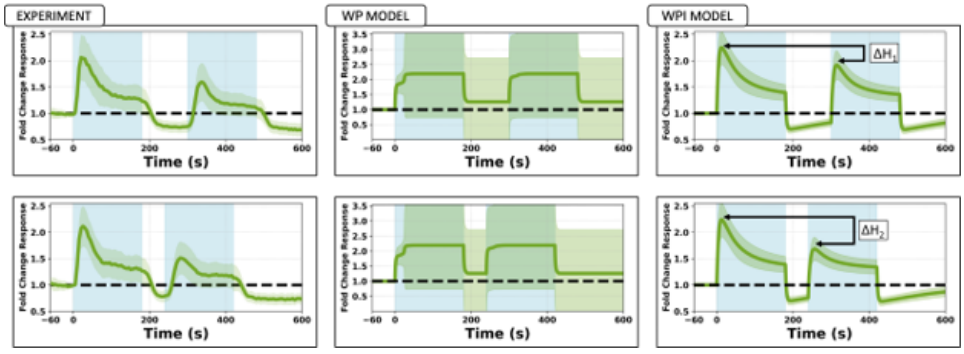

Figure 2.2: Data from Town and Weiner [47] (left) and model fits by the WP model (centre, $n = 58$) and the WPI model (right,$n = 81$). Mean Active Rac (solid green curves) ± 1 SD (green shading). Light blue represents stimulus ON phase. Top: a longer delay ($\Delta t_1 = 120s$). Both models were independently fit to the data from the longer delay ($\Delta t_1 = 120s$) experiment. Bottom: A short delay, ($\Delta t_2 = 60s$) between stimuli. The results for the shorter delay ($\Delta t_2 = 60s$) were generated as predictions, using the fitted parameters. The longer delay leads to smaller difference in amplitudes ($\Delta H_1 < \Delta H_2$). The WPI, but not the WP model, accounts for these experimental features. The WP model fails to capture the heterogeneity of the data, resulting in a wider spread. This also reduced the number of successful fits from a total of 81 (successful WPI model fits) to only 58 (for WP).

2.3 Response to Gradual Versus Rapid Stimulation

I asked how the WPI model responds to a gradual "ramp-up" stimulus instead of the sharp ON–OFF pulses. The predictions of the WPI model, along with the corresponding experimental results, are shown in Figure 2.3. As seen in the bottom row, the model predicts a controlled rise in Rac activity without the overshoot observed in response to pulse stimuli (top row of the same figure). However, the model also shows a slight increase in Rac activity above pre-stimulus levels, in contrast to experimental data, where Rac remains close to baseline. This behaviour together with the overshoot of Rac in sharp pulse stimuli is referred to as adaptation.

Adaptive systems exhibit a transient response before returning to a low level. According to Ma et al. [27], there are two types: (1) perfectly adaptive systems, which restore output to its original value after input, and (2) imperfectly adaptive systems, which partially decay but do not fully return to baseline. In terms of a dynamical system, perfectly adaptive systems are those where the steady state of a variable is independent of some input, while imperfectly adaptive systems are dependent on it in some form.

The discrepancy between the experimental results and simulated results in the bottom row of Figure 2.3 highlights a limitation of the WPI model: while it achieves adaptation, it is not perfectly adaptive under all conditions. The experimental data suggest that the biological system more closely approaches perfect adaptation, particularly under slowly varying inputs. Despite this difference, the results support the idea that the inhibitor acts as a filter, allowing the cell to respond preferentially to rapid changes rather than to gradual shifts or absolute levels of stimulation.

2.4 Fitting Parameters to Data

Table 2.1 summarizes the best-fit values of the ODE model parameters obtained by the fitting algorithm called **Differential Evolution** [40]. I used only the double-pulse experiment shown in the top row of Figure 2.2 (for $\Delta t_1 = 120s$) to fit parameters and then simulated the other cases with the parameter set thus obtained. This resulted in 81 individual cells for which I ran the fitting routine independently, this is shown in the spread of parameter ranges; such spread of fitted parameters reflects the heterogeneity in Rac activity dynamics observed across cells.

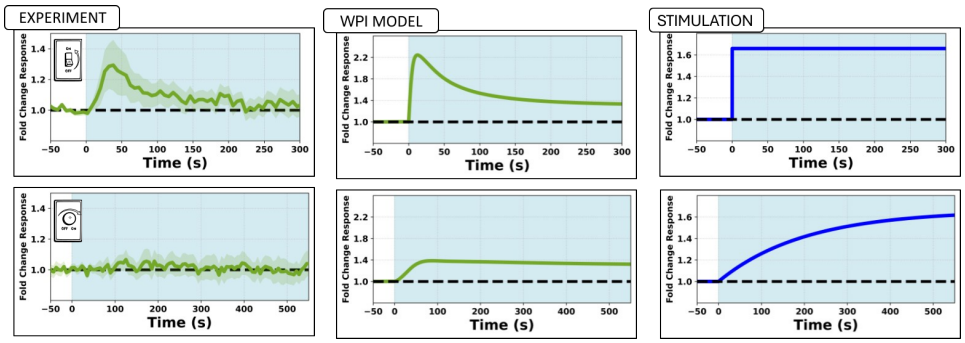

Figure 2.3: Responses to ON (Top) versus ramp stimuli (Bottom). The WPI model distinguishes between abrupt and gradual stimuli (Centre). A step-function stimulus (Top) triggers an overshoot in Rac activity, followed by adaptation, in agreement with experiments [47] (Left). A gradual stimulus (Bottom) leads to a mild Rac increase above baseline (in contrast with the baseline data) with no overshoot. The findings suggest that the Rac inhibitor filters stimuli, reacting to rapid, rather than gradual changes.

2.4.1 Differential Evolution Overview

I used the built-in SciPy algorithm [42] to find a minimum of a cost function within a bounded parameter space. The algorithm works as follows:

- Given the lower and upper bounds for each parameter (say n parameters), sample N non-identical vectors in $\mathbb{R}^n$. Sampling is performed using Latin hypercube sampling to ensure the samples are well distributed.
- Form the mutant group by randomly selecting 3 different vectors, one serves as the base, to which a fraction of the difference between the other two is added, producing a new set of N vectors.
- Perform crossover between the mutant group and the original group. For each parameter, select the mutant value to replace the original with a given probability, ensuring at least one parameter is always mutated. This generates a new family of N vectors mutated from the original group.
- For each new individual, compare their cost function values. If the mutation results in a lower cost, accept the mutant, otherwise, keep

the original. This produces a new generation of parameter sets, and the process is repeated.

Using this routine, I fitted the ODEs in Equation (2.2) and Equation (2.3), normalizing the results by setting the pre-stimulus level of active Rac to a baseline of 1. For each individual cell, I had access to both its active Rac responses and its PIP3 time course. To better capture heterogeneity, I replaced the input term $S(t)$ with the measured PIP3 data $p_{\text{data}}(t)$. Here $p_{\text{data}}(t)$ represents the experimentally recorded PIP3 signal, obtained from biofluorescence imaging rather than simulation. To normalize these measurements, we divided the fluorescence intensities by the average pre-stimulation signal across the cell, thereby setting the pre-stimulus baseline to 1. Unlike $S(t) \in [0, 1]$, $p_{\text{data}}(t)$ can exceed 1. The parameter α_p scales the effect of PIP3 in this setting.

In the WP model that yields:

$$\frac{du}{dt} = (T - u)\left(k_0 + \alpha_p p_{\text{data}}(t) + \gamma \frac{u^n}{K^n + u^n}\right) - \delta u, \tag{2.4}$$

While for the WPI model I have:

$$\begin{aligned} \frac{du}{dt} &= (T - u)\left(k_0 + \alpha_p p_{\text{data}}(t) + \gamma \frac{u^n}{K^n + u^n}\right) - (\delta + k_1 h)u, \\ \frac{dh}{dt} &= k_h u - \delta_h h, \end{aligned} \tag{2.5}$$

2.4.2 Fitting Results

Overall, the fitting results show that the basal Rac activation rate, k_0 is much lower than the autocatalytic rate γ, and that Rac inactivation δ is higher in the WP model that has no inhibitor. As a result, total Rac is higher in WP than WPI due to differences in adaptation dynamics, and the inhibitor in WPI decays much more slowly than Rac itself. This is the first time that experimental data is being used to fit parameters to the WP model (since the Mori et al 2008 paper [32]), and results of the fits are highly consistent with ball-park estimates made in that purely theoretical model. More details can be found in the appendix.

It would be interesting to compare the parameter values with others from the literature, but the number of previous model fits to data is quite limited. Lockley et al [25, 26] fit three polarity models [22, 30, 34] to F-actin data from Dictyostelium cells repolarizing in response to reversal of a shear

flow. These models do not specifically identify molecular components, but both Meinhardt's [30] and Otsuji's [36] models have an "active" variable. Otsuji [36] considers active and inactive forms of the protein, with mass conservation, as does the Mori et al [32] WP model, though other details differ significantly.

Parameters	**WP**	**WPI**
T (Total Rac) [AU]	9.78 ± 0.70	7.31 ± 0.28
k_0 (Basal Rac activation rate) [1/s]	0.035 ± 0.006	0.028 ± 0.003
α_p (Stimulus-induced Rac activation rate) [1/s]	0.12 ± 0.03	0.059 ± 0.006
γ (Autocatalytic Rac activation rate) [1/s]	1.31 ± 0.10	1.38 ± 0.084
K (Hill-function half-maximal activation threshold) [AU]	2.75 ± 0.19	2.93 ± 0.16
δ (Basal Rac inactivation rate) [1/s]	2.70 ± 0.11	0.721 ± 0.027
k_1 (Inhibitor-induced Rac inactivation) [1/s]	—	0.372 ± 0.026
k_h (Rac-dependent inhibitor production rate) [1/s]	—	$6.8 \times 10^{-3} \pm 4.0 \times 10^{-4}$
δ_h (Inhibitor decay rate) [1/s]	—	$4.0 \times 10^{-3} \pm 6.0 \times 10^{-4}$

Table 2.1: Fitted parameter values for the WP ($\text{residuals}^2 = 4183.57, n = 58$) and WPI ($\text{residuals}^2 = 615.19, n = 81$) models. "[AU]" represents arbitrary units. The stated values and ranges represent a 95% confidence level given the distribution of fitted parameters. The Hill coefficient for Rac autocatalysis was kept fixed at $n = 2$. Time is in seconds (s). Data and models are scaled so that active Rac is normalized (given as fold-multiples of its basal prestimulus level). Each cell has its own PIP3 level (used as proxy for input stimulus) and its own normalized Rac activity level. The inhibitor is in arbitrary units [AU]. For details about the fitting routine, see Appendix.

2.4.3 Selection of Best Fit Time-Dependent Model

The WPI model has three parameters more than the WP model, as seen in Table 2.1. We asked whether the WPI model is a better parsimonious fit to the data despite this increase in degrees of freedom. To address this

question, we used the Akaike Information Criterion (AIC) [2], one of the ways to assess model performance. AIC rewards a low sum of squared errors (SSE) and penalizes the number of parameters in comparing distinct models fit to the same dataset. According to the AIC results (Table 2.2), the WPI model provides a significantly lower AIC score, which indicates a better fit to the data, more than compensating for the penalty of adding three additional parameters. The details of how we computed the AIC score are given in Appendix A.4.2.

Model	**AIC**	**ΔAIC**	**AIC Weight**	**RSS**	**Samples (n)**
WPI	938.6	0	≈ 1.00	3707.5	425
WP	1160.3	221.7	≈ 0.00	6335.8	425

Table 2.2: Model selection. Akaike Information Criterion (AIC) model comparison using the best-fit parameters for the temporal data corresponding to the $120s$ gap. The AIC values were calculated using observations from all time-points ($30s$, $60s$, $120s$, $240s$, and $480s$), highlighting that the WPI model provides a significantly better fit to the data than the WP model. Here, ΔAIC denotes the difference from the best (lowest) AIC, thus 0 for WPI

Chapter 3

Spatial Dynamics

3.1 Main Puzzle

Throughout this work, the reaction-diffusion models are implemented on a 1D spatial stationary domain with periodic boundary conditions, which represents the cell edge as viewed from above. This domain simulates a closed loop around the perimeter of the cell, and spatial coordinates are given in fixed "lab coordinates": 0° points upwards (north), $+90^\circ$ to the left (west), -90° to the right (east), and $\pm 180^\circ$ downwards (south), as shown in Figure 1.2.

As previously shown in Figure 1.4, embedding the WP full PDE model in a Cellular Potts model (CPM) framework allowed me to replicate several responses that cells have to simple light stimulation protocols, such as steering toward the stimulus, executing U-turn trajectories when stimulated at the rear, and maintaining a single front even under competing stimuli. However, when replicating the local-to-global experiment shown in the middle and right columns of Figure 1.5 the WP model fails to show the reversal of direction of rotation observed experimentally. Instead, the simulated cells persist along a straight path once the stimulus becomes spatially uniform. This outcome highlights a key limitation of the WP model: In the absence of spatial cues, the location of peak Rac activity tends to remain fixed, with no mechanism to sustain the cell's prior rotation or reverse its direction of motion. These results are shown in Figure 3.1.

The initial hypothesized answer to how to account for this reversal trajectory was that by adding the inhibitor, we should be able to give this adaptive feature to the model. Since the parameter fitting shows that the inhibitor reacts on a different timescale than Rac, this could allow the cell to adapt differently when going from a local to a global stimulus, as only portions of the cell would have a high concentration of inhibitor, preserving a spatial bias even when the stimulus is set uniform. In this chapter I will explore different responses of the WPI model in its full spatio-temporal version.

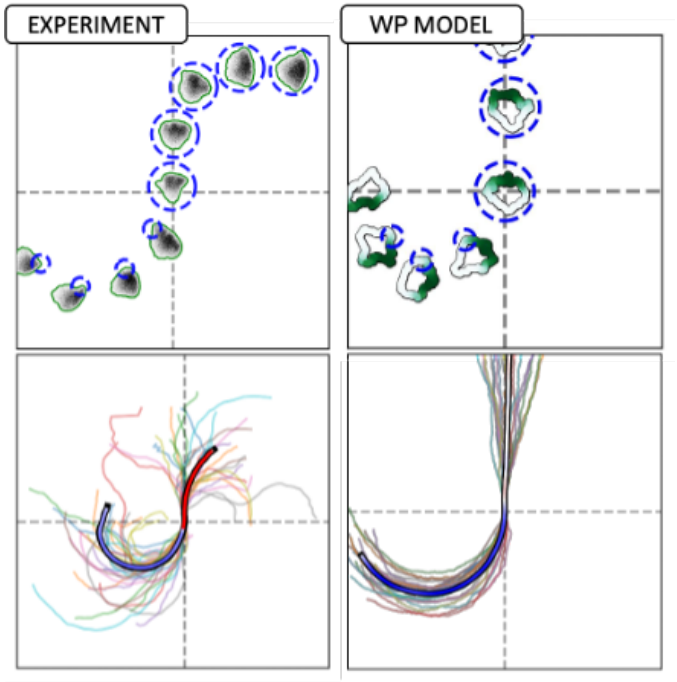

Figure 3.1: Cells stimulated by local optogenetic inputs followed by global stimulation first turn in one direction, then reverse. Experimental data [47] (left panels) show the directional behaviour and trajectories of cells, with snapshots (top left) and tracked positions (bottom left). The Wave-Pinning [32] (WP) model (right panels) reproduces the initial turning behaviour but not the reversal under global stimuli, showing cell shapes and trajectories (top right) and summarized paths (bottom right). In the lower panels, all individual cell tracks are shown (25 for the experiment, 20 for the WP model), with the average trajectory overlaid and colour-coded by rotation direction: blue for counterclockwise (CCW), red for clockwise (CW), and white for no rotation. Experimental data adapted from Town and Weiner [47]. Notably, while experimental cells reverse and begin turning CW after global stimulation, WP model cells continue along a straight trajectory.

3.2 WPI Responds More Strongly to Sudden Stimuli Than to Gradual Stimuli

After exploring how the WPI model responds to different rates of stimulation in time, I next investigated how those temporal dynamics translate into spatial behaviour along the cell edge. As previously mentioned, I returned to the spatial (PDE) version of the model, where the cell edge is represented as a one-dimensional stationary domain with periodic boundary conditions, defined by $x \in [-180°, +180°]$, with $x = -180°$ identified with $x = +180°$, with $D_u \ll D_v$ to allow polarized solutions. Now $S(x,t)$ depends on space and time, allowing me to replicate local stimulation protocols.

$$\frac{\partial u}{\partial t} = v\left(k_0 + \alpha S(x,t) + \gamma \frac{u^n}{K^n + u^n}\right) - (\delta + k_1 h)\, u + D_u \frac{\partial^2 u}{\partial x^2}, \tag{3.1a}$$

$$\frac{\partial v}{\partial t} = -v\left(k_0 + \alpha S(x,t) + \gamma \frac{u^n}{K^n + u^n}\right) + (\delta + k_1 h)\, u + D_v \frac{\partial^2 v}{\partial x^2}, \tag{3.1b}$$

$$\frac{\partial h}{\partial t} = k_h u - \delta_h h + D_h \frac{\partial^2 h}{\partial x^2}, \tag{3.1c}$$

I then simulated the system's response to two types of spatially localized stimuli: one introduced abruptly as a step-function, and the other gradually ramped over time. The step and ramp profiles mirror the global, non-motile-cell experiments in Figure 2.3. Here I apply them locally and add a competing local stimulus, which has not been tested experimentally.

In both simulations, the cell was first subjected to a constant local stimulus at $x = -90°$. At $t = 100s$, a second stimulus was applied at $x = +90°$, either as an instantaneous pulse or as a gradual ramp (top and bottom rows of Figure 3.2, respectively). I captured both the stimulation pattern and active Rac levels in kymographs shown in Figure 3.2, which display their spatial profiles over time along the 1D domain. Figure 3.2 also includes a metric comparing the average stimulation across two regions: from $x = -180°$ to $x = 0°$, referred to as the "Previously Stimulated" side, and from $x = 0°$ to $x = +180°$, referred to as the "Naive Side." Although both sites eventually received the same maximal stimulus intensity, the responses of the system were markedly different.

In the case of the pulse input, Rac activity rapidly reoriented, shifting from the original site at $x = -90°$ to the new stimulus at $x = +90°$. However, when the new stimulus was applied gradually, Rac activity remained at its original location, and the new zone failed to form. These results indicate that the WPI model does not simply integrate stimulus magnitude

over time but instead filters inputs based on their rate of change.

This behaviour highlights the role of the inhibitor in shaping the model's response: rapid inputs overcome the inhibitory suppression and trigger reorientation, while slow changes are dampened, allowing the original Rac zone to persist. Unlike the WP model, where reorientation depends on stimulus strength or duration, the WPI model responds selectively to fast changes. This filtering mechanism could be critical in guiding cell movement in dynamic environments, enabling cells to ignore weak or slowly varying cues and focus on sharp, directional changes.

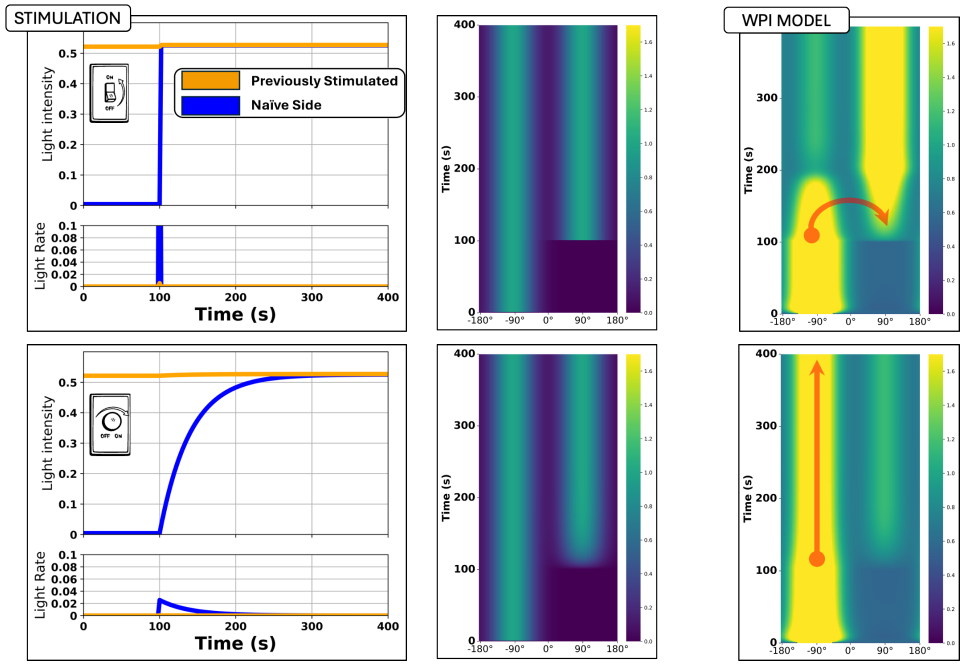

Figure 3.2: The WPI model distinguishes abrupt (top) from gradual (bottom) stimuli. Cells were first exposed to constant light on one half, the Previously Stimulated side (orange). A second stimulus was applied to the opposite Naive side (blue), either as a step or ramp. For each protocol, three plots are shown: the leftmost compares average light intensity and rate of change on both sides (after $t = 100$, curves coincide, so blue is hidden); the centre is a kymograph of the light stimulus (space: $x = -180°$ to $x = +180°$, time in seconds, lighter = higher intensity); the rightmost is the corresponding Rac kymograph with the same axes and colour scheme. Abrupt stimuli redirected Rac; gradual stimuli did not.

3.3 After Stimulation, Cells With WPI Continue Rotating

I implemented the models' signalling systems along the 1D cell edge and linked Rac activity to protrusion as described earlier.

Here, I applied a more dynamic stimulation protocol. Rather than fixing the stimulus location in space, I updated its position so that it always remained $+90°$ counterclockwise from the cell's direction of motion. In other words, as the cell moved and reoriented, the stimulus was always kept at a fixed position relative to the cell's front. This setup ensured that the stimulus persistently guided the cell into a turning motion, as illustrated in Figure 3.3. Once the cell's front aligned with the northward direction, the stimulus was turned off. As discussed before, Rac activity responds more quickly than the inhibitor, and this difference in timing leads to a spatial lag, so that the inhibitor trails behind the Rac zone. This trailing effect pushes Rac along the domain, effectively sustaining the cell's turning motion even after the stimulus is removed.

3.4 Summary of Findings

In summary, I found that the WPI model maintains cell rotation even after the light stimulus is removed, due to the lag between the Rac front and its associated inhibitor. This temporal separation allows the cell to continue turning in the same direction for a while, even after the stimulus is removed, effectively preserving its prior behaviour. I also showed that the WPI model responds differently depending on how quickly a stimulus is applied, reacting strongly to abrupt changes but filtering out gradual ones. However, these features are still not sufficient to explain the surprising reversal of polarity observed in the local-to-global stimulus experiment. This result contradicts the original hypothesis by Town and Weiner, who proposed that an inhibitor alone could account for the reversal, suggesting that something is still missing from the model. This puzzle is the focus of the next chapter.

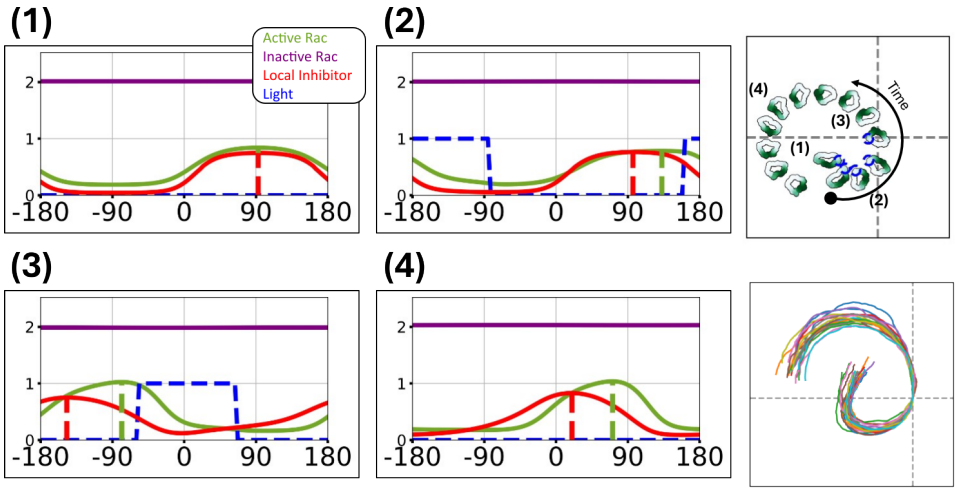

Figure 3.3: The WPI model is shown, implemented on the "unwrapped" 1D cell edge (left four panels) and on a CPM simulation in Morpheus (Right). (Left) Four time points showing spatial profiles of active and inactive Rac (green, purple, respectively), the Rac inhibitor (red), and the light stimulus (blue). The peaks of active Rac and inhibitor are indicated (dashed lines). (Top right) Snapshots of the simulated motile cell moving in 2D at corresponding time points. Active Rac is shown in green shading, and blue circles indicate light stimulus. The inhibitor trails behind Rac, sustaining a persistent rotation of the cell. Time points denote (1) period before stimulation, (2,3) periods of direct stimulation, (4) periods after stimulation.

Chapter 4

The Reversal Experiment

4.1 WPI Does Not Account for Reversal Experiment

The core puzzle addressed by Town and Weiner [47] is the counterintuitive reversal of cell rotation following a shift from local to global stimulation. In their experiments, cells stimulated locally on their left side began rotating counterclockwise, similar to the initial setup in Figure 3.3. However, once the stimulus was switched to a global input, most cells reversed direction and rotated clockwise.

Town and Weiner originally hypothesized that introducing an inhibitor would be sufficient to reproduce the reversal observed in the local-to-global stimulus experiment. Based on this, I tested whether the WPI model could account for the behaviour. My reasoning was based on two observations from earlier results. First, as shown in Figures 2.2 and 3.2, the WPI model is sensitive to the rate of stimulation, suggesting that sudden changes in input could strongly affect Rac dynamics. Second, spatially localized stimulation, even when overlapping with an existing Rac zone, can give rise to competing zones that potentially reorient polarity.

I expected that switching from local to global stimulation would create a sharp rate increase on the right side of the cell, where there had previously been no signal, while the left side, already stimulated, would see no change. Since the WPI model responds strongly to sudden increases, I hypothesized that this asymmetry would favour Rac activation on the right and trigger reversal of the direction of rotation.

To test this, I implemented a stimulation protocol matching that of the experiments. I began with local stimulation on the "left side" of the cell (90° counterclockwise from the cell's front), inducing a counterclockwise rotation. When the cell's front points north (0°), I abruptly switched the stimulus to a uniform global illumination. This transition should have created a large rate of Rac activation 90° clockwise from the current front, potentially initiating reversal. To mimic biological variability, I ran simulations using a range of

parameter sets drawn from my previously fitted pool, thereby generating a population of trajectories.

Contrary to my expectations, the WPI model did not produce polarity reversal. Instead, cells continued rotating counterclockwise, despite the switch to global stimulation. Figure 4.1 shows the evolution of Rac activity and inhibitor distribution along the cell edge in a representative simulation. Peaks of Rac and inhibitor (third panel: green and red lines, respectively) reveal that the inhibitor lags behind Rac but ultimately reinforces its persistence.

Although the right side of the cell experiences a strong and sudden increase in Rac activation rate during the switch to global stimulus, the effect is short-lived. The inhibitor, which decays slowly, continues to suppress Rac in that region, preventing the emergence of a new front. As a result, the initial Rac zone remains dominant, and the cell does not reverse direction.

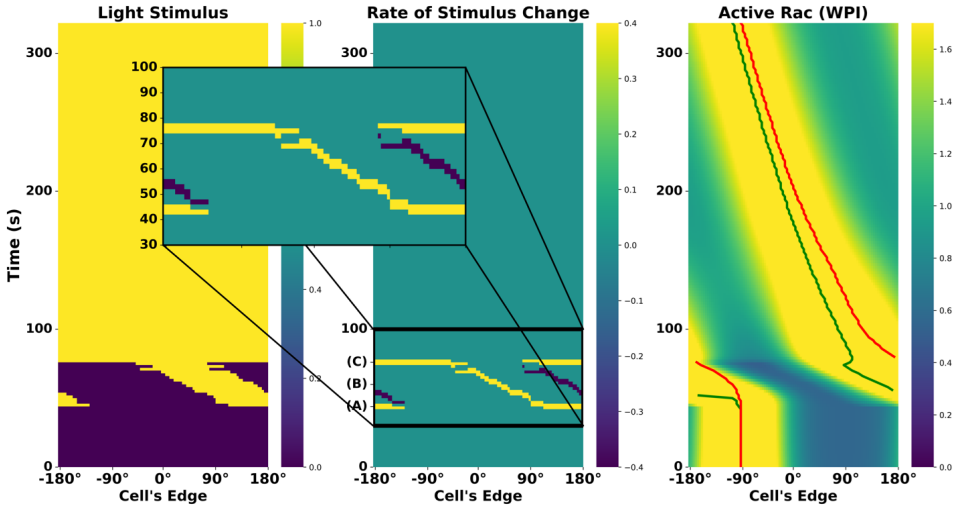

Figure 4.1: Left to right: kymographs of light stimulus, its rate of change, and active Rac. The zoom-in highlights three key moments as shown on the time axis of the central plot: (A) onset of local stimulation, (B) transient phase during rotation, and (C) switch to global stimulation. The WPI model fails to reverse Rac polarity following global stimulus, despite a sharp rate of change at the back of the active zone. Green and red curves in the right panel track the peak positions of Rac and the inhibitor, respectively.

4.2 WPI-PIP3 Model

Having established that the WPI model alone fails to capture the experimentally observed reversal (Figure 4.1), I sought a minimal extension that could explain this behaviour. My previous results (Figures 2.2 and 3.2) demonstrated that Rac redistribution is sensitive to the rate of stimulus change, but in Figure 4.1, I saw that this effect alone was not sufficient to drive the reverse in rotation. Instead, Rac persisted in its original rotation.

In Town and Weiner's experiments, Rac was not directly activated by light but instead through the PI3K-PIP3 pathway (see Figure 1.7 C). PI3K, recruited by illuminated receptors, catalyzes the production of the lipid PIP3 at the membrane. PIP3, in turn, has been shown to enhance Rac activation. This upstream component provides a biologically motivated extension to the WPI framework. By simulating PIP3 dynamics explicitly, I introduce a time lag between light input and Rac activation, which proves crucial for reproducing the reversal behaviour.

I denote the level of PIP3 by $p(x,t)$ and assume it is produced, in response to light stimulus, from a finite pool of membrane lipids available to form PIP3:

$$\frac{\partial p}{\partial t} = (T_p - p)\left(k_p + \beta S\left(x,t\right)\right) - \delta_p p + D_p \frac{\partial^2 p}{\partial x^2}, \tag{4.1a}$$

where the model parameters are: T_p (size of the total lipid pool available for conversion to PIP3), k_p (basal PIP3 production rate), β (light stimulus intensity to PIP3 production rate), δ_p (basal PIP3 degradation rate), and D_p (PIP3 diffusion rate). The Rac activation term is then modified by replacing the direct light term $S(x,t)$ with a dynamic PIP3 input. The new system of equations becomes (4.1a) and:

$$\frac{\partial u}{\partial t} = v\left(k_0 + \alpha_p p(x,t) + \gamma \frac{u^n}{K^n + u^n}\right) - \left(\delta + k_1 h\right) u + D_u \frac{\partial^2 u}{\partial x^2}, \tag{4.1b}$$

$$\frac{\partial v}{\partial t} = -v\left(k_0 + \alpha_p p(x,t) + \gamma \frac{u^n}{K^n + u^n}\right) + \left(\delta + k_1 h\right) u + D_v \frac{\partial^2 v}{\partial x^2}, \tag{4.1c}$$

$$\frac{\partial h}{\partial t} = k_h u - \delta_h h + D_h \frac{\partial^2 h}{\partial x^2}. \tag{4.1d}$$

This system forms the WPI–PIP3 model. The key idea is that PIP3's dynamics introduces a time delay between light input and Rac activation.

4.3 WPI-PIP3 Reproduces Simple Turning Behaviour

I verified that WPI-PIP3 retains the ability to reproduce the basic cell turning behaviours that were originally captured by the WP model. These include the U-turns observed under rear stimulation and directional turning in response to one or two stimulation sites on the L and R cell sides.

Here, I repeat those protocols using the WPI-PIP3 models with its best-fit parameters. As shown in Figure 4.2, the model produces qualitatively correct turning behaviour: In the rear-stimulation, most of the time the cell makes a U-turn and then moves in the opposite direction. In the one-sided stimulus, the model cell turns towards the stimulus direction, while in the two-sided stimuli, the cell randomly selects a "winning" direction, as seen in the experiments.

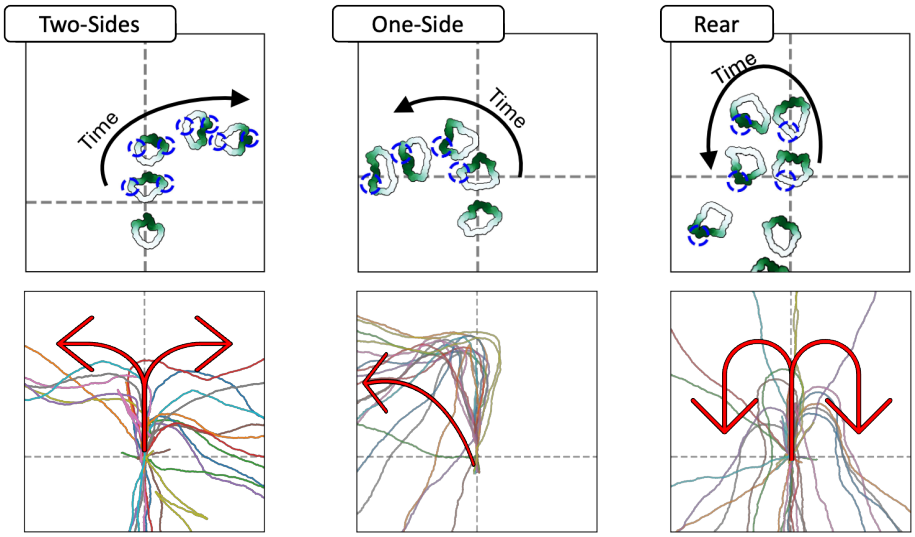

Figure 4.2: Each column shows results from a distinct stimulus: two-sided stimulation (left), one-sided (middle), and rear stimulation (right). Top row: Representative snapshots from simulated cell trajectories over time. Active Rac is shown in green, light stimulus in blue. Bottom row: Superimposed tracks of 20 simulated cells in response to each stimulus. Red arrows indicate typical direction of turning.The WPI-PIP3 model captures the expected behaviour in each case: random left/right choice under two-sided stimulation, directional turning under one-sided stimulation, and a U-turn under rear stimulation.

4.4 Fitting Spatial Rac Polarization Data to Motile Cells

To fit spatial data, I extracted the distribution of Rac activity along the cell's edge from the data of Town and Weiner, producing a 1D periodic domain that can be directly compared to the results of the WPI-PIP3 model. This allowed me to fit the diffusion rate parameters (Table 4.1), while keeping the previous fitted kinetic parameters in Table 2.1. I report relative diffusion ratios normalized to the active Rac diffusion rate (set to 1). Physical units, scaling details, and protocol-specific fitting procedures are provided in Appendix A.4.5. Similar to the previous fitting, our results aligned with theoretical expectations: (1) The diffusion rate of active Rac is found to be small, while inactive Rac has a much larger diffusion coefficient (approximately 6.4-fold higher). (2) The hypothesized inhibitor has a diffusion rate lower than that of active Rac, reinforcing its local nature.

Parameters	**WPI**	**WPI-PIP3**
D_u (Active Rac diffusion rate)	1	1
D_v (Inactive Rac diffusion rate)	3.37	6.40
D_h (Inhibitor diffusion rate)	0.14	0.47

Table 4.1: Setting the diffusion coefficient of active Rac to $D_u = 1$ (in arbitrary units), we scaled all other diffusion coefficients relative to D_u. Fitting was performed across all spatial stimulation protocols ($n = 166$), using the average Rac profile within each protocol. As expected, we found that inactive Rac diffuses faster than active Rac. We also found that the inhibitor diffuses most slowly. See Appendix A.4.5 for correspondence to unit-carrying values and for further details.

4.5 Lag Due to PIP3 Explains Reversal

The WPI-PIP3 model successfully reproduces the polarity reversal observed in the local-to-global stimulus experiment, as shown in Figures 4.3 and 4.4. Among the models I tested here only the WPI-PIP3 captures the switch in rotation direction after global stimulation, consistent with experimental results. Having a parametrized set of models allows me to ask what features of the expanded WPI-PIP3 model account for the reversal and under what conditions. In Appendix A.3, I describe a sequence of in-silico experiments that help to pinpoint the necessary conditions and how interactions between

the components lead to reversal. Briefly, I show that (1) PIP3 adds a lag that maintains the influence of the local stimulus for a short while during global stimulation. (2) If PIP3 dynamics are too fast or too slow, there is no reversal. (3) Indeed, the cell's reversal depends on a delicate balance between all parameters. When I sample parameter sets from my fitted distributions (mimicking biological heterogeneity), I observe cases where reversal does not occur, in agreement with experimental results. I briefly summarize these observations in Figures 4.3 and 4.4 and show details in Appendix A.3.

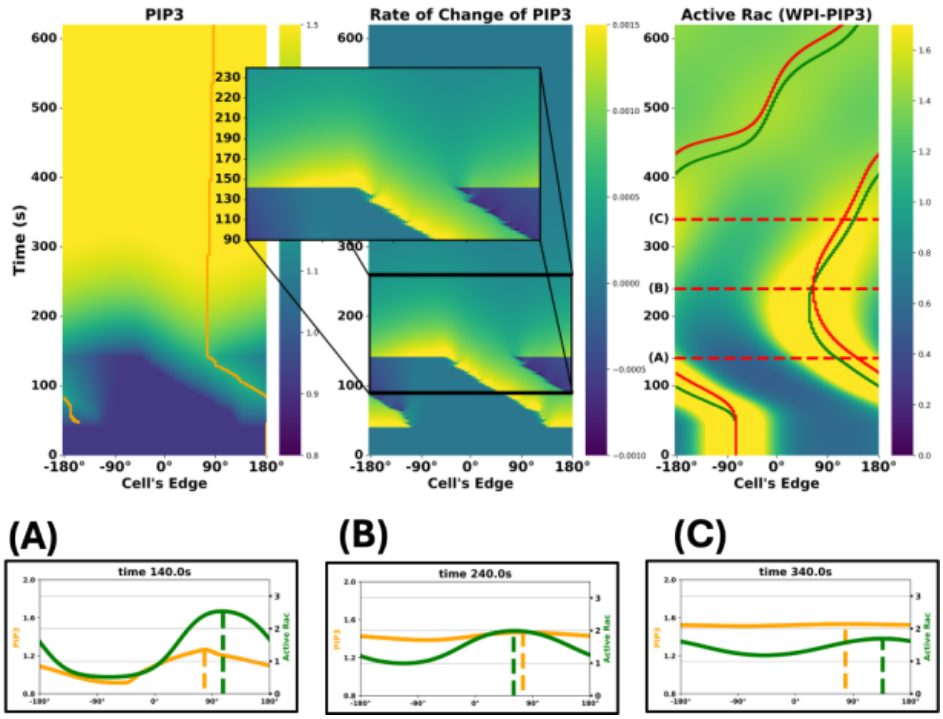

Figure 4.3: (Top) Kymographs of: PIP3 concentration (Left), PIP3 rate of change (Centre), and active Rac (Right), with orange, green, and red curves tracking the peaks of PIP3, Rac, and inhibitor, respectively. Time points (on kymograph, right and bottom row): (A) Global stimulus turned on, (B) Rac and PIP3 peaks switch positions initiating the reverse rotation, (just before the inhibitor catches up, not shown), (C) reverse rotation is stabilized and sustained. The spatial profiles of PIP3 (orange) and active Rac (green) are shown at corresponding time points (bottom row). Dashed lines denote peaks of PIP3 and Active Rac.

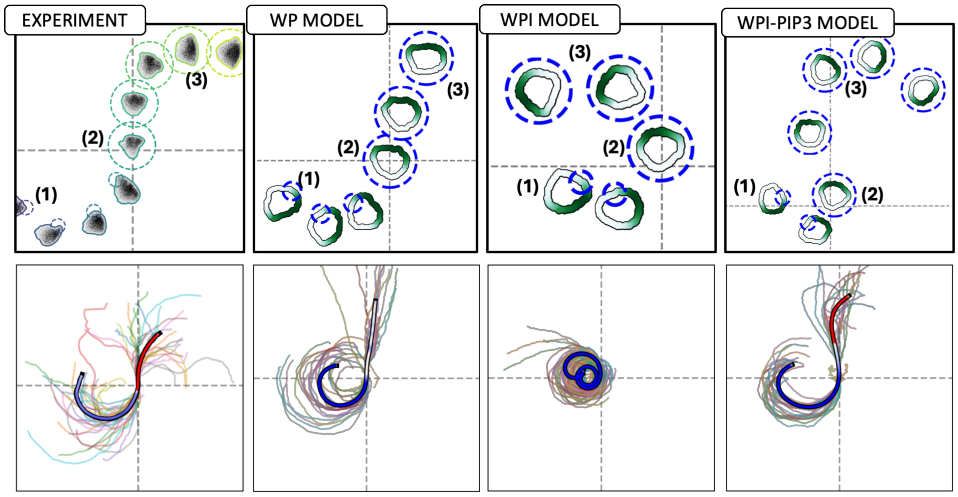

Figure 4.4: A comparison of cell shapes, active Rac distributions along the cell edge (green) and various cell trajectories in the experiment (left) and in cell simulations predicted by the three models (L to R: WP, WPI, and WPI-PIP3) with heterogeneous parameters. In the lower panels, all individual cell tracks are shown (25 for the experiment, 20 for each of the models), with the average trajectory overlaid and colour-coded by rotation direction: blue for counterclockwise (CCW), red for clockwise (CW), and white for no rotation. In all models, the cell is first locally stimulated on its left from $t = 100$ to $t = 300$, triggering counterclockwise rotation. At $t = 300$, global stimulus is turned on. WP predicts straight migration or loss of polarity and stalling; WPI continues its initial rotation; Only WPI-PIP3 reverses direction, matching experimental results.

Chapter 5

Model Cell Responses to Dynamic and Noisy Gradients

While previous simulations focused on optogenetic protocols, neutrophils in-vivo respond to chemical gradients, not light. To evaluate how well the WP, WPI, and WPI-PIP3 models perform in more realistic environments, I tested their behaviour in virtual chemical fields. In practice, this meant simulating CPM cells exposed to a 2D chemical field that could be static, shifting, or noisy, rather than to optogenetic light inputs. This allowed me to ask what advantages the additional components in WPI and WPI-PIP3 offer when cells navigate changing or noisy gradients. I designed two benchmark simulations: one that tests the cell's ability to reorient when the gradient shifts, and another that tests how well the cell can maintain directed motion under different levels of spatial noise. These types of experimental conditions can be challenging to control in vitro, but simulations provide a way to explore how each component contributes to robust guidance.

In this setting, the external attractant is defined as a static gradient over the entire simulation space. To simulate the next results, I assume that the function $S(x, t)$ represents the chemical concentration sensed by the cell at position x along its edge. This is defined as the intersection between the cell edge and a predefined, static chemical gradient over the simulation space, and it determines the local Rac activation rate used in the model. As mentioned, this replaces the optogenetic light stimulus previously used.

I performed two benchmark simulations to test responses predicted by the three signalling models (WP, WPI, WPI-PIP3): (i) The ability of cells to follow an initial (noise-free) gradient and to respond to gradient reversal, and (ii) the ability to follow a noisy gradient. The noise was generated by adding random values sampled from a normal distribution with mean zero and varying standard deviation (ranging from 0 for no noise, to 0.4 and 0.8). Negative values were clipped to zero to ensure all stimulus values remained

non-negative.

5.1 Noise-free Environment, With Gradient Reversal

I simulated a scenario where cells are initially placed in a northward pointing chemical gradient. At $t = 80$, the chemical field is briefly reset to uniform, followed by gradient reversal at $t = 120$. As shown in Figure 5.1, all three models (WP, WPI, and WPI-PIP3) initially polarize and undergo chemotactic migration up the gradient. Based on my fitted parameters, I found that the WP model predicts delayed polarization onset compared with WPI and WPI-PIP3, particularly in regions of low chemoattractant concentration. Upon gradient reversal, the inhibitor models (WPI and WPI-PIP3) successfully reoriented. WP remained fixed in its original direction. WPI cells showed a slower reversal, as shown by their short reversal paths. In contrast, WPI-PIP3 cells reversed more rapidly, producing longer reversed trajectories.

The differences in the models can be explained as follows. First, the inhibitor accumulates at the front and destabilizes the Rac zone there. This destabilization facilitates the replacement of the existing front, making reversal more likely. Second, the faster reorientation in the WPI-PIP3 model arises from the PIP3 dynamic adaptation to the changing gradient. After the gradient reverses, PIP3 redistributes from a previously high level, decreasing across the cell, but more slowly in the direction of the new gradient. This creates an early asymmetry that facilitates a faster response.

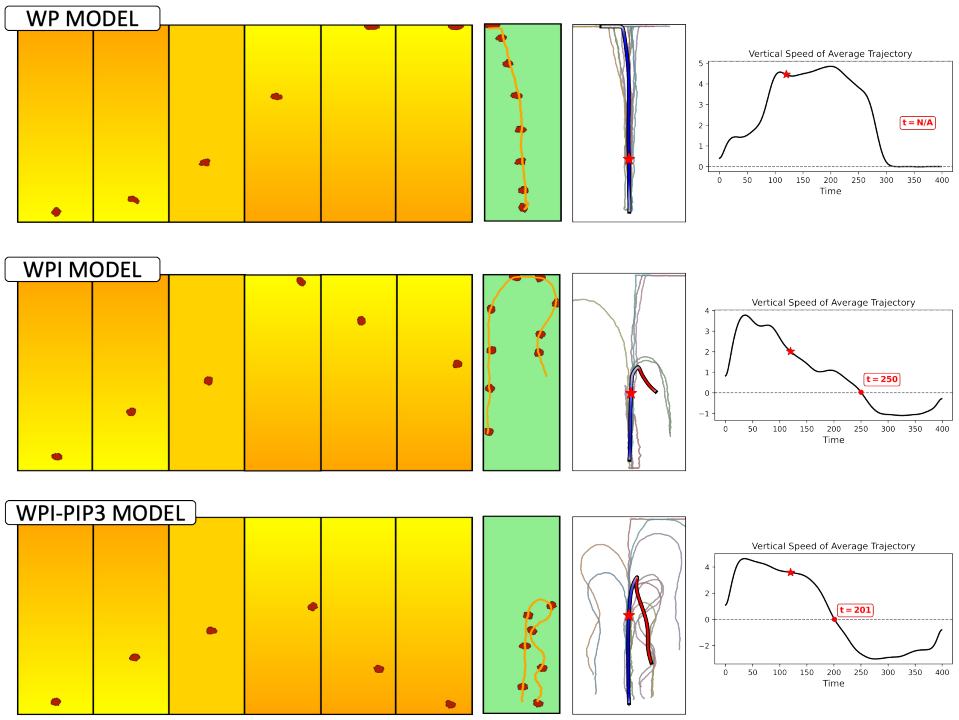

Figure 5.1: Predicted sensitivity of the three types of model cells to dynamic chemical gradients. Left six panels: snapshots of cell positions (red shapes) and chemical gradient from low (yellow) to high (orange) concentrations. In a noise-free gradient, eventually all cells align with the initial gradient. WP (top) polarizes very slowly and fails to reorient after gradient reversal. In contrast, WPI and WPI-PIP3 (middle and bottom) polarize faster and successfully reverse direction after the gradient flips. Green and white panels: single representative cell trajectory, followed by a sample of several. The blue-red coloured track indicates the average path taken by the cells. The colour changes from blue (Northwards direction) to red (Southwards direction), with a red star marking the gradient reversal time point. Right panel: average vertical velocity vs time (with the same red star); the red dot indicates the cell reorientation time, (undefined for the WP model). Notably, WPI-PIP3 reorients faster ($t = 201$) than WPI ($t = 250$). The sudden drop in WP vertical speed is due to the cell reaching the top boundary of the domain, not active reorientation.

5.2 Response to Noisy Chemical Fields

To evaluate the efficiency of the models in aligning the cell's polarity with a noisy gradient, I tested all three models (WP, WPI, and WPI-PIP3) with a fixed (northward) chemical gradient on which various levels of spatial noise were superimposed. I simulated 20 cells for each configuration of model and noise level, and the cell's direction (determined by Rac zone) was averaged. Results are shown in Figure 5.2. In a noise-free gradient, all model cells successfully aligned with the gradient, as previously observed. However, as noise variance increased, the WP model exhibited poor performance. While the WPI model performed better than WP, it struggles to align in the presence of high noise levels. The WPI-PIP3 model demonstrates the best performance. I believe that the presence of PIP3, which acts as an intermediary between the chemical stimulus and Rac activation, allows the cell to smooth out noisy stimuli. This highlights not only the importance of the inhibitor but also the role of upstream components, such as PIP3 that allow the cell to process noisy stimuli more effectively. In effect, PIP3 acts as a filter: while it perceives the noisy fluctuations in the chemical field, its dynamics smooth out these momentary variations, allowing the cell to respond more reliably to the underlying gradient.

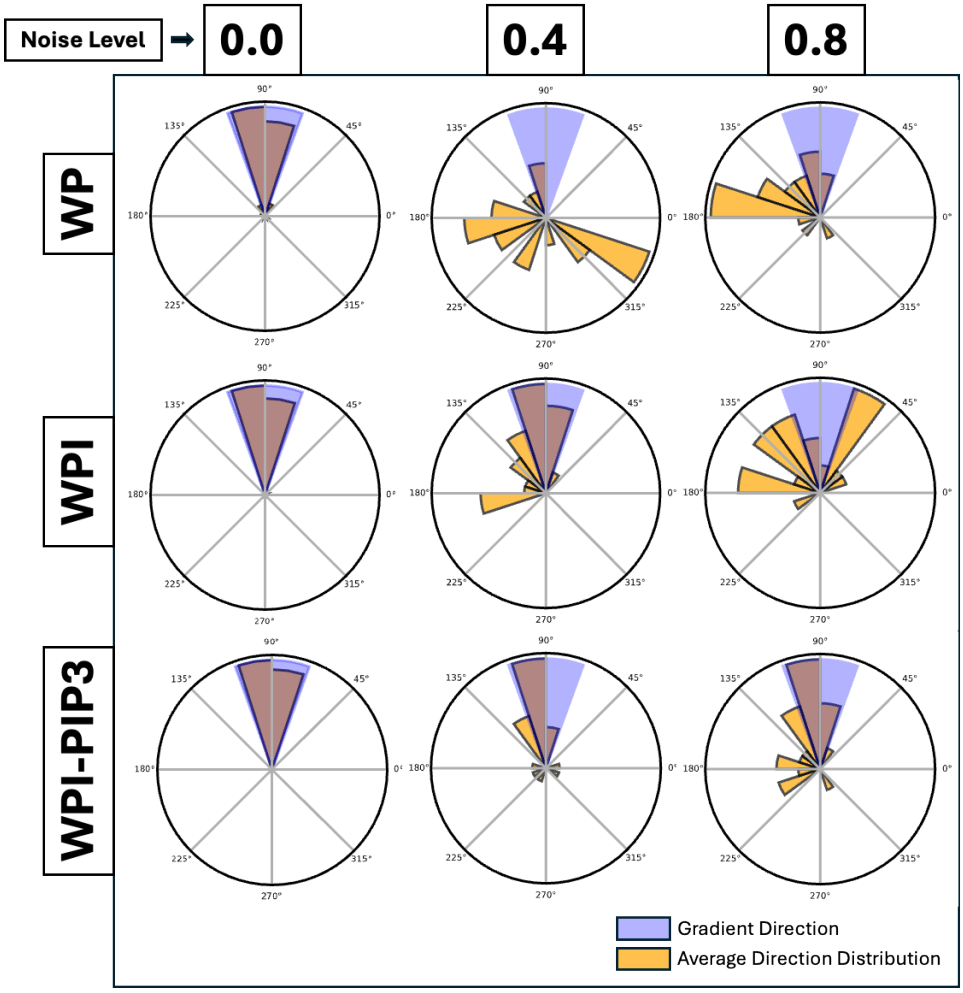

Figure 5.2: Each row corresponds to a model (top to bottom: WP, WPI, WPI-PIP3), and each column represents a level of noise added to the gradient (left: none, middle: moderate, right: high). All models align well with a gradient without noise, but only the WPI-PIP3 allows the cell to sense highly noisy gradients. Noise level indicates the standard deviation of the added noise.

5.3 PIP3 Alone Does Not Account for Success in Noisy Gradients

To validate that the success of the WPI-PIP3 model in noisy environments (as shown in Figure 5.2) requires the combined action of both the inhibitor and PIP3, I tested a fourth model variant containing only the WP mechanism and PIP3, but no inhibitor (WP-PIP3).

Figure 5.3 shows the predicted response of this model variant to the same noisy gradients previously tested. As noise variance increases, the model rapidly loses its ability to align with the gradient. Despite the smoothing effect of PIP3, the absence of a local inhibitor impairs the cell's ability to detect a weak noisy gradient. This result supports the conclusion that both components are required for robust chemotaxis in complex environments.

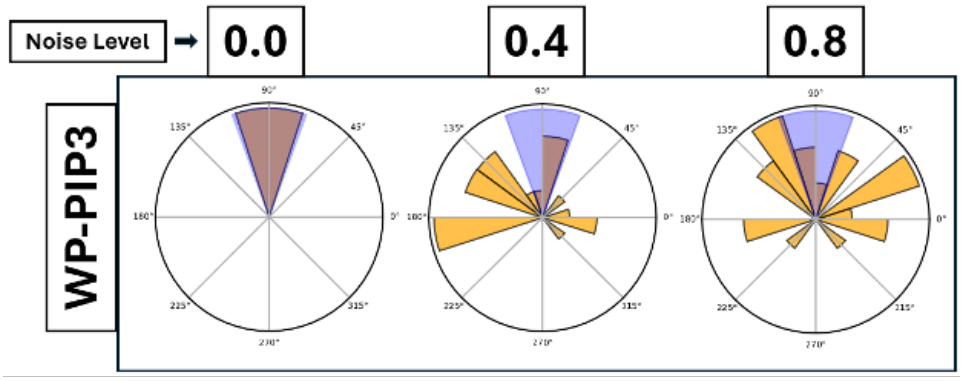

Figure 5.3: As in Figure 5.2, but for the model with no inhibitor (WP-PIP3). Each rose plot shows the distribution of averaged Rac polarity directions in cells stimulated with a fixed northward gradient at various levels of noise (standard deviation = 0.0, 0.4, 0.8). The models align well in the absence of noise, but its performance degrades rapidly under increasing noise, demonstrating the role of the Rac-inhibitor in robust gradient sensing.

Chapter 6

Discussion

In this study, I developed and analyzed a series of biologically grounded models for Rac activation and polarization in neutrophils. My main contribution is to provide a modelling framework that validates a key experimentally-based hypothesis proposed by Town and Weiner [47]: that a local Rac inhibitor is required to explain responses to optogenetic stimuli. Through a systematic investigation of several model variants, I demonstrated and explained the roles of a Rac inhibitor and of PIP3 in accounting for responses to various stimulation protocols, the reversal experiment. These results show that combining a local inhibitory mechanism with a slow-adapting intermediate (PIP3) provides a robust and minimal mechanism for flexible polarity responses in neutrophils.

6.1 Key Findings and Biological Implications

The behaviours observed in my simulations suggest several biological implications. Most notably, I find that the ability to reorient in response to changing cues, such as a switch from local to global stimulation or a gradient reversal, requires both a local inhibitor and a dynamic "filtering" component such as PIP3. The inhibitor plays a primary role in enabling redirection by destabilizing the current front. PIP3 further enhances reorientation by smoothing stimulus transitions and preserving a directional bias after abrupt changes. This extended adaptive behaviour helps the system avoid erratic responses, particularly in noisy environments. Together, the inhibitor and PIP3 work in concert, to provide a basic biologically plausible mechanism for robust polarity control in migrating cells.

6.2 Relation to Activator–Inhibitor Models

The diffusion rates we obtained (Table 4.1) invite comparison with activator–inhibitor frameworks. In classical Turing systems, pattern formation arises when an activator diffuses slowly and is counterbalanced by a more

rapidly spreading inhibitor. Our fitted parameters differ from this expectation: the inhibitor diffuses more slowly than active Rac, highlighting its strongly local action. Thus, while the model shows some resemblance to activator–inhibitor ideas, it does not rely on a Turing-type mechanism.

6.3 Relation to Previous Models

Although this work has been focused on neutrophil cellular migration, this model could be generalized to other amoeboid cells with similar signalling networks such as *Dictyostelium* [38, 50]. Several modelling studies have previously explored the dynamics of cell polarity and migration using reaction–diffusion systems coupled to deformable domains. The model most closely related to mine is that of Neilson et al. [34], who introduced a pseudopod activator together with local and global inhibitors in PDEs defined on a closed curve representing the edge of a motile cell. Their framework has the advantage of incorporating curvature and membrane-tension effects into the dynamics, but their activator and inhibitors were not intended to correspond to specific molecular species. In contrast, my formulation replaces these abstract variables with Rac GTPase, introduces a local inhibitory feedback supported by experiments, and is parameterized directly from live-cell data.

Other important contributions include the multiscale models of Marée et al. [28, 29], which combined Rho-family GTPases with actin-driven protrusions to explain keratocyte motility (with extensions analysing PI feedback and shape–signalling interactions), and the work of Vanderlei et al. [48], who coupled reaction–diffusion polarity to deformable cell boundaries to study feedback between signalling and shape. In parallel, Niculescu et al. [35] extended the Cellular Potts Model with an actin-inspired local positive-feedback mechanism that yields amoeboid and keratocyte-like migration in multicellular settings, providing a computationally light, shape-driven framework rather than an explicit reaction–diffusion biochemical model. Compared with these, my approach maintains a deforming-edge geometry but emphasizes a minimal Rac–inhibitor–PIP3 circuit constrained by experiments, thereby complementing mechanically focused and phenomenological models with a signalling-centred perspective.

More recent extensions of the wave–pinning framework have also highlighted the diversity of possible polarity behaviours. Liu et al. [24] embedded wave–pinning models into a Cellular Potts framework to classify patterning regimes and cell shapes, while Camley et al. [4] used a phase-field approach

to couple biochemical polarity to deformable shapes. Unlike these surveys, my work focuses on identifying and testing specific feedback circuits against experimental Rac dynamics.

Taken together, this study extends the tradition of cell-edge PDE frameworks such as Neilson et al. by embedding a data-driven Rac–inhibitor–PIP3 feedback network. It complements multiscale, mechanical, and shape-driven models by providing a signalling-focused framework that is directly constrained by experiments, situating Rac regulation within the broader family of polarity and motility models.

6.4 Parameter Fitting

There are several interesting aspects of the fitted parameter in Table 2.1: (1) The basal Rac activation rate (k_0) is small, and much smaller than the elevated rate when Rac is autoactivating itself ($k_0 \ll \gamma$). Indeed, the basal rate is around 3% of the elevated activation rate ($k_0 \approx 0.027\gamma$). This is required to assure a low resting-level of Rac activity that can get significantly elevated by positive feedback. (2) The basal rate of Rac inactivation (δ) is considerably higher (by 3.75-fold) in the WP model that has no inhibitor. This is reasonable, since in the WPI model, much of the work of damping out Rac activity is accomplished by the putative inhibitor. (3) The level of total Rac (T) is larger in the WP model than in the WPI (34%). This difference can be understood by realizing that for long periods of stimulation, WP holds a steady level of activation, while WPI rises and then falls (following adaptation). Hence when fitting the models to data, WP was forced to balance between the peak and the long-term Rac activity, resulting in fits that favour higher values of the Rac activation rates. On the other hand, WPI can reach high peaks immediately after stimulation, followed by lower long-term activity thanks to the slow inhibitor time dynamics. (4) In the WPI model, the rate of decay of the inhibitor (δ_h) is significantly lower ($< 1\%$) than the rate of decay of Rac. This implies that the inhibitor persists for much longer (half-life $= \ln(2)/0.0040 \approx 173s$), compared to Rac (half-life $= \ln(2)/0.721 \approx 1s$). (5) This is the first time that experimental data is being used to fit parameters to the WP model (since the Mori et al 2008 paper [32]), and results of the fits are highly consistent with rough estimates made in that purely theoretical model. In particular, it was noted there and in Hughes et al [17] that a nonzero basal rate of Rac activation ($k_0 > 0$) is theoretically essential for polarity by the WP mechanism to exist, but that it should be very small compared to the autocatalytic rate of Rac

activation due to the positive feedback of Rac ($k_0 \ll \gamma$). The fits to the WP model, confirm this theory, even while the WPI model is seen to be a better fit to the neutrophil stimuli experiments.

6.5 Estimating Molecular Properties of the Inhibitor

The rate of diffusion of the inhibitor was found to be smaller than that of active Rac. Using the Stokes-Einstein relation [31] and the diffusion ratio of 1.0:0.47 (active Rac : inhibitor) we get $D \propto \frac{1}{MW^{1/3}}$ implying that the inhibitor could have MW roughly $(1.0/0.47)^3 = 9.6$ times that of Rac. Since typical small GTPases are around 21 kDa, this implies the inhibitor MW is on the order of 200 kDa. This estimate, along with comparisons to known GAPs such as ARHGAP5 (172 kDa) and MYO9B (243 kDa), was informed by discussion with Town & Weiner, hence the putative inhibitor could be a GAP. Alternately, the inhibitor could have protein-binding domains that lead to formation of complexes around that size, also a feature known in GAPs, or it could be sequestered by the cytoskeleton, which would reduce its mobility. My parameter fitting results also imply that the inhibitor is recruited (or activated) at a very low rate by Rac, while also having a very slow rate of inactivation relative to Rac kinetics. These results may eventually lead to further identification of the likely molecular candidate(s) playing the role of the Rac inhibitor.

6.6 Strengths of This Approach

While previous studies provide important insights into self-organization and shape change, my work differs in three key ways. First, I test specific hypotheses about the molecular circuit underlying polarity reversal, using both time-dependent simulations and cell motility simulations to account for experimental observations. Second, rather than relying solely on hand-tuned parameters, my model is quantitatively calibrated to experimental data, enabling me to extract parameter distributions across cells and thereby account for biological heterogeneity. Third, my use of the Morpheus platform makes the full CPM model openly accessible and easily reproducible, lowering the barrier for further exploration and validation.

6.7 Model Limitations and Future Directions

While my model reproduces key aspects of polarity reversal and directional adaptation, it simplifies several biological processes. In particular, the dynamics are simulated in a one-dimensional periodic domain, which removes a degree of freedom for molecular movement and approximates the true deforming cell edge by a fixed circle. This Morpheus shortcut does not capture the feedback between cell shape changes and intracellular dynamics that has been demonstrated in other models [28, 43]. I also do not include mechanical feedback from membrane tension, which has been shown to act as a global inhibitor of Rac dynamics [16, 49].

The intracellular dynamics are further simplified, focusing on a minimal Rac–inhibitor–PIP3 circuit and omitting additional regulators such as Rho or Cdc42 [13, 23, 43]. These simplifications allow me to isolate and test the minimal requirements for polarity reversal, but they also highlight natural directions for refinement.

One promising avenue would be to move beyond the stationary circular domain and adopt a bulk–surface PDE framework as developed by Cusseddu et al. [6], combined with the surface-evolution approach of Elliott et al. [9]. Implementing my WPI and WPI-PIP3 models within such a deforming-domain setting would provide a more realistic representation of feedback between Rac signalling, PIP3 dynamics, and cell shape.

Bibliography

[1] Jupiter Algorta, Jason P. Town, Orion D. Weiner, and Leah Edelstein-Keshet. Investigating local negative feedback of Rac activity by mathematical models and cell motility simulations. *bioRxiv*, May 2025. Preprint.

[2] Kenneth P. Burnham, David R. Anderson, and SpringerLink (Online service). *Model Selection and Multimodel Inference: A Practical Information-Theoretic Approach*. Springer, New York, 2nd;2;2.; edition, 2002;2010;.

[3] Andreas Buttenschön, Yue Liu, and Leah Edelstein-Keshet. Cell size, mechanical tension, and GTPase signaling in the single cell. *Bulletin of Mathematical Biology*, 82(2):28, 2020.

[4] Brian A. Camley, Yanxiang Zhao, Bo Li, Herbert Levine, and Wouter-Jan Rappel. Crawling and turning in a minimal reaction-diffusion cell motility model: Coupling cell shape and biochemistry. *Physical Review. E*, 95(1):012401–012401, 2017.

[5] Hao Chang and Andre Levchenko. Adaptive molecular networks controlling chemotactic migration: dynamic inputs and selection of the network architecture. *Philosophical Transactions of the Royal Society of London. Series B. Biological Sciences*, 368(1629):20130117–20130117, 2013.

[6] Davide Cusseddu and Anotida Madzvamuse. Numerical investigations of the bulk-surface wave pinning model. *Mathematical Biosciences*, 354:108925, 2022.

[7] Henry De Belly, Andreu Fernandez Gallen, Evelyn Strickland, Dorothy C. Estrada, Patrick J. Zager, Tamas L. Nagy, Janis K Burkhardt, Hervé Turlier, and Orion D. Weiner. Long range mutual activation establishes rho and rac polarity during cell migration. *bioRxiv*, 2025.

[8] Henry De Belly, Shannon Yan, Hudson Borja da Rocha, Sacha Ichbiah, Jason P. Town, Patrick J. Zager, Dorothy C. Estrada, Kirstin Meyer, Hervé Turlier, Carlos Bustamante, and Orion D. Weiner. Cell protrusions and contractions generate long-range membrane tension propagation. *Cell*, 186(14):3049–3061.e15, 2023.

[9] Charles M. Elliott, Björn Stinner, and Chandrasekhar Venkataraman. Modelling cell motility and chemotaxis with evolving surface finite elements. *Journal of the Royal Society Interface*, 9(76):3027–3044, 2012.

[10] François Graner and James A. Glazier. Simulation of biological cell sorting using a two-dimensional extended potts model. *Physical Review Letters*, 69(13):2013–2016, 1992.

[11] Brian R. Graziano, Delquin Gong, Karen E. Anderson, Anne Pipathsouk, Anna R. Goldberg, and Orion D. Weiner. A module for Rac temporal signal integration revealed with optogenetics. *The Journal of Cell Biology*, 216(8):2515–2531, 2017.

[12] Gurkan Guntas, Ryan A. Hallett, Seth P. Zimmerman, Tishan Williams, Hayretin Yumerefendi, James E. Bear, and Brian Kuhlman. Engineering an improved light-induced dimer (iLID) for controlling the localization and activity of signaling proteins. *Proceedings of the National Academy of Sciences - PNAS*, 112(1):112–117, 2015.

[13] Amalia Hadjitheodorou, George R. Bell, Felix Ellett, Shashank Shastry, Daniel Irimia, Sean R. Collins, and Julie A. Theriot. Directional reorientation of migrating neutrophils is limited by suppression of receptor input signaling at the cell rear through myosin II activity. *Nature Communications*, 12(1), 2021.

[14] Richard G. Hodge and Anne J. Ridley. Regulating Rho GTPases and their regulators. *Nature Reviews Molecular Cell Biology*, 17(8):496–510, 08 2016.

[15] W. R. Holmes, A. E. Carlsson, and L. Edelstein-Keshet. Regimes of wave type patterning driven by refractory actin feedback: transition from static polarization to dynamic wave behaviour. *Physical Biology*, 9(4):46005–046005, 2012.

[16] Andrew R Houk, Alexandra Jilkine, Cecile O Mejean, Rostislav Boltyanskiy, Eric R Dufresne, Sigurd B Angenent, Steven J Altschuler, Lani F Wu, and Orion D Weiner. Membrane tension maintains cell

polarity by confining signals to the leading edge during neutrophil migration. *Cell*, 148(1-2):175–188, 2012.

[17] J. M. Hughes, S. Modai, L. Edelstein-Keshet, and A. Yochelis. Travelling waves and wave pinning (polarity): Switching between random and directional cell motility. *arXiv preprint*, 2024.

[18] Takanari Inoue and Tobias Meyer. Synthetic activation of endogenous PI3K and Rac identifies an and-gate switch for cell polarization and migration. *PloS One*, 3(8):e3068, 2008.

[19] Tian Jin. Gradient sensing during chemotaxis. *Current Opinion in Cell Biology*, 25(5):532–537, 2013.

[20] Toshiyuki Kakumoto and Takao Nakata. Optogenetic control of PIP3: PIP3 is sufficient to induce the actin-based active part of growth cones and is regulated via endocytosis. *PloS One*, 8(8):e70861, 2013.

[21] Elzbieta Kolaczkowska and Paul Kubes. Neutrophil recruitment and function in health and inflammation. *Nature Reviews. Immunology*, 13(3):159–175, 2013.

[22] Andre Levchenko and Pablo A. Iglesias. Models of eukaryotic gradient sensing: Application to chemotaxis of amoebae and neutrophils. *Biophysical Journal*, 82(1):50–63, 2002.

[23] Benjamin Lin, William R. Holmes, C. J. Wang, Tasuku Ueno, Andrew Harwell, Leah Edelstein-Keshet, Takanari Inoue, and Andre Levchenko. Synthetic spatially graded Rac activation drives cell polarization and movement. *Proceedings of the National Academy of Sciences - PNAS*, 109(52):E3668–E3677, 2012.

[24] Yue Liu, Elisabeth G. Rens, and Leah Edelstein-Keshet. Spots, stripes, and spiral waves in models for static and motile cells: GTPase patterns in cells. *Journal of Mathematical Biology*, 82(4):28, 2021.

[25] Robert Lockley. *Image-based modelling of cell reorientation.* PhD thesis, University of Warwick, 2015.

[26] Robert Lockley, Graham Ladds, and Till Bretschneider. Image based validation of dynamical models for cell reorientation. *Cytometry. Part A*, 87(6):471–480, 2015.

[27] Wenzhe Ma, Ala Trusina, Hana El-Samad, Wendell A. Lim, and Chao Tang. Defining network topologies that can achieve biochemical adaptation. *Cell*, 138(4):760–773, 2009.

[28] Athanasius F. M. Marée, Verônica A. Grieneisen, and Leah Edelstein-Keshet. How cells integrate complex stimuli: The effect of feedback from phosphoinositides and cell shape on cell polarization and motility. *PLoS Computational Biology*, 8(3):e1002402, 2012.

[29] Athanasius F. M. Marée, Alexandra Jilkine, Adriana Dawes, Verônica A. Grieneisen, and Leah Edelstein-Keshet. Polarization and movement of keratocytes: A multiscale modelling approach. *Bulletin of Mathematical Biology*, 68(5):1169–1211, 2006.

[30] H. Meinhardt. Orientation of chemotactic cells and growth cones: models and mechanisms. *Journal of Cell Science*, 112(17):2867–2874, 1999.

[31] Christina C. Miller. The Stokes-Einstein law for diffusion in solution. *Proceedings of the Royal Society of London. Series A*, 106(740):724–749, 1924.

[32] Yoichiro Mori, Alexandra Jilkine, and Leah Edelstein-Keshet. Wave-pinning and cell polarity from a bistable reaction-diffusion system. *Biophysical Journal*, 94(9):3684–3697, 2008.

[33] William M. Nauseef and Niels Borregaard. Neutrophils at work. *Nature Immunology*, 15(7):602–611, 2014.

[34] Matthew P. Neilson, Douwe M. Veltman, Peter J. M. van Haastert, Steven D. Webb, John A. Mackenzie, and Robert H. Insall. Chemotaxis: A feedback-based computational model robustly predicts multiple aspects of real cell behaviour. *PLoS Biology*, 9(5):e1000618, 2011.

[35] Ioana Niculescu, Johannes Textor, and Rob J. de Boer. Crawling and gliding: A computational model for shape-driven cell migration. *PLoS Computational Biology*, 11(10):e1004280, 2015.

[36] Mikiya Otsuji, Shuji Ishihara, Carl Co, Kozo Kaibuchi, Atsushi Mochizuki, and Shinya Kuroda. A mass conserved reaction–diffusion system captures properties of cell polarity. *PLoS Computational Biology*, 3(6):e108, 2007.

[37] Chiara Pantarelli and Heidi C. E. Welch. Rac-GTPases and Rac-GEFs in neutrophil adhesion, migration and recruitment. *European Journal of Clinical Investigation*, 48(S2):e12939–n/a, 2018.

[38] Kyung C. Park, Francisco Rivero, Ruedi Meili, Susan Lee, Fabio Apone, and Richard A. Firtel. Rac regulation of chemotaxis and morphogenesis in dictyostelium. *The EMBO Journal*, 23(21):4177–4189, 2004.

[39] Marten Postma, Leonard Bosgraaf, Harriët M. Loovers, and Peter J M Van Haastert. Chemotaxis: signalling modules join hands at front and tail. *EMBO Reports*, 5(1):35–40, 2004.

[40] Kenneth Price. *Differential Evolution: A Practical Approach to Global Optimization*. Springer Nature, Berlin, Heidelberg, 1 edition, 2006;2005;.

[41] Elisabeth G. Rens and Leah Edelstein-Keshet. Cellular tango: how extracellular matrix adhesion choreographs Rac-Rho signaling and cell movement. *Physical Biology*, 18(6):66005, 2021.

[42] SciPy Community. scipy.optimize.differential_evolution — scipy v1.13.0 manual. `https://docs.scipy.org/doc/scipy/reference/generated/scipy.optimize.differential_evolution.html`, 2024.

[43] Changji Shi, Chuan-Hsiang Huang, Peter N. Devreotes, and Pablo A. Iglesias. Interaction of motility, directional sensing, and polarity modules recreates the behaviors of chemotaxing cells: e1003122. *PLoS Computational Biology*, 9(7), 2013.

[44] Adam Shutes, Cercina Onesto, Virginie Picard, Bertrand Leblond, Fabien Schweighoffer, and Channing J. Der. Specificity and mechanism of action of EHT 1864, a novel small molecule inhibitor of Rac family small GTPases. *The Journal of Biological Chemistry*, 282(49):35666–35678, 2007.

[45] Jörn Starruß, Walter de Back, Lutz Brusch, and Andreas Deutsch. Morpheus: a user-friendly modeling environment for multiscale and multicellular systems biology. *Bioinformatics*, 30(9):1331–1332, 2014.

[46] Jared E. Toettcher, Delquin Gong, Wendell A. Lim, and Orion D. Weiner. Light-based feedback for controlling intracellular signaling dynamics. *Nature Methods*, 8(10):837–839, 2011.

[47] Jason P. Town and Orion D. Weiner. Local negative feedback of Rac activity at the leading edge underlies a pilot pseudopod-like program for amoeboid cell guidance. *PLoS Biology*, 21(9):e3002307, 2023.

[48] Ben Vanderlei, James J. Feng, and Leah Edelstein-Keshet. A computational model of cell polarization and motility coupling mechanics and biochemistry. *Multiscale Modeling Simulation*, 9(4):1420–1443, 2011.

[49] Cole Zmurchok, Jared Collette, Vijay Rajagopal, and William R. Holmes. Membrane tension can enhance adaptation to maintain polarity of migrating cells. *Biophysical Journal*, 119(8):1617–1629, 2020.

[50] Marko Šoštar, Maja Marinović, Vedrana Filić, Nenad Pavin, and Igor Weber. Oscillatory dynamics of Rac1 activity in dictyostelium discoideum amoebae. *PLoS Computational Biology*, 20(12):e1012025, 2024.

Appendix A

Modelling Methods

A.1 Model Geometry

I use two frames of reference, the lab coordinates, and a coordinate system along the cell edge. In lab coordinates, 0^o is taken to be in the "North" direction, for convenience, and most simulations start with cells polarized in that direction. I also consider a cell-based coordinate system to describe positions along the cell edge. "Front" then denotes the location of maximal Rac activity on the edge, rear is at the opposite pole of the cell, and right or left sides are at $\pm\pi/2$ radians from the front location.

The cell frame of reference moves relative to lab coordinates. As the cell moves, stimuli in [47] were computer-controlled to be fixed relative to this inherent cell framework. (Hence, for example, "stimulating on the left" always implies a stimulus at $-\pi/2$ from the "front".)

In the models described below, I use $-180 \leq x < 180$ to denote the lab frame of reference, analogous to a lab "compass". Hence, as the cell reorients due to stimuli, the Rac zone (as well as the stimulus, and all other variables) will appear to "shift" relative to this frame of reference.

A.2 The Cellular Potts Model (CPM) Simulations

To simulate cell motility driven by Rac dynamics, I implemented the model equations Equation (3.1) and Equation (4.1) on the edge of a 2D deformable simulated cell in Morpheus (Starruß et al., [45]). Morpheus is an open source multiscale modelling platform for simulating single and collective cell behaviour, based on the Cellular Potts Model (CPM).

CPM cells are represented by a connected set of pixels with a fluctuating edge that can randomly protrude or retract at each point. An energetic cost function (the "Hamiltonian") prevents the total area and/or perimeter of the CPM cell from deviating away from a user-specified target area (A_0) and perimeter (P_0). These constraints are weighted by strengths λ_a, λ_p set

by the user. In general, I set $\lambda_a = 1, \lambda_p = 1$, and pick P_0 as a fold-multiple, ϕ, of the perimeter of a circle with area A_0. The constant ϕ denoted the "Aspherity", describes the deviation of a cell shape from that of a perfect circle. In general,

$$\text{Aspherity} = \frac{P}{2\sqrt{\pi A}},$$

where P is the perimeter and A the area of the cell. For a perfect circle, this ratio equals 1. Values greater than 1 indicate increasingly elongated or irregular cells shapes. (I found $\phi \approx 1.4 - 1.46$ to be consistent with shapes of neutrophils.) The Morpheus software allows all such parameters to be easily specified. For fuller details about the Cellular Potts Model, see [10].

While previous custom-built CPM code represented PDEs for GTPase activity inside 2D deforming CPM cells [29, 41], in open-source software such as Morpheus, this type of simulation is not yet available. However, the Morpheus plugin `MembraneProperty` allows users to solve reaction-diffusion equations such as WP in a periodic 1D stationary domain representing the "cell edge"[1].

The RD system is implemented in Morpheus using the `DiffEqn` plugin, which allows direct numerical integration of PDEs on domains such as the cell edge. To couple the Rac activity to protrusion at points along the cell's edge, I used the Morpheus plugin `StarConvex`; this plugin allows me to favour protrusive pixel fluctuations at locations along the cell-edge with high Rac activity (high u). This idea is consistent with localized nucleation of F-actin downstream of active Rac, and hence, protrusion associated with high Rac activity zones. Furthermore, to represent implicit "persistence", with gradual (rather than instantaneous) cytoskeletal turnover (while not explicitly tracking F-actin in the model), I used the Morpheus `Protrusion` plugin. This plugin implements the "Act" idea of Niculescu et al. [35] [2], enabling the cell to sustain and amplify the protrusions caused by `StarConvex`.

The edge distribution of active Rac is solved on a discretized 1D lattice using the sequential operator splitting method. In Morpheus, these are built-in solver options: diffusion is computed using the central difference method, and reactions are updated using Euler time-stepping.

[1] In actual fact, Morpheus solves such problems on a circular domain with the same area as the CPM cell, and then "projects" the solution values along radii from the cell's centroid to its perimeter.

[2] As in [35], newly added pixels are assigned a fixed "actin level" (ACT) that decays over time, creating a memory of recent protrusive activity. The CPM Hamiltonian is biased to favour copy attempts from high-activity pixels to neighbouring low-activity pixels, mimicking actin-driven edge protrusion.

A.3 Mechanism of Rotation Reversal in the WPI-PIP3 Model

Because PIP3 production is driven by light, it accumulates within the Rac zone during local stimulation, forming a nonuniform pattern with a peak. When the stimulus switches to a global stimulus, this localized PIP3 peak does not immediately dissipate. Instead, it persists briefly, creating a transient spatial bias.

Immediately after I switch to the global stimulus, Rac continues its counterclockwise rotation, driven by the delayed peak of the inhibitor, which sustains the previous motion. However, as Rac progresses, it leaves behind the PIP3 peak that formed during local stimulation. This lingering PIP3 peak locally enhances Rac activation and effectively pulls Rac back toward it, acting as a temporary "anchor point" or attractor. As a result, Rac slows down and eventually reverses direction. By the time PIP3 becomes uniform across the cell, Rac has already reoriented and the inhibitor, now trailing the shifted Rac, helps maintain the reversed rotation.

I tested this mechanism in two ways:

- **Constant inhibitor:** To isolate the role of adaptive feedback, I removed the dynamic inhibitor and set its effect to a constant value. This essentially reduces the system back to a WP-like regime, with Rac inactivation fixed across space and time. During local stimulation, Rac slowly shifts towards the stimulus site. However, upon switching to global stimulation, memory of the previous stimulation is entirely lost. The Rac zone then stalls at its last position and maintains a stable front. This mirrors behaviour seen in the standard WP model and confirms that a dynamic inhibitory response is necessary for directional change (Figure A.1)

- **PIP3 Rate variation:** To test the sensitivity of the model to PIP3 dynamics, I altered the PIP3 timescale in the full WPI-PIP3 model (with dynamic inhibitor). Results in Figure A.2 demonstrate that for fast PIP3 dynamics, PIP3 quickly becomes uniform across the domain. Once global stimulation is applied, without any lingering asymmetry, Rac experiences a spatially uniform stimulus from PIP3 and continues rotation under the influence of the inhibitor, effectively behaving like the WPI model. On the other hand, for very slow PIP3 dynamics, the PIP3 peak remains localized for too long, acting as a fixed attractor. Rac is unable to fully pass or disengage from it, resulting in oscillatory

motion around the PIP3 peak rather than a clean reversal.

These tests demonstrate that reversal depends on a fine balance between a delayed, localized inhibitor and a transient, asymmetric PIP3 signal. If either component is missing or mistimed, the system either fails to reverse (WPI-like) or becomes trapped, losing polarity (WP-like).

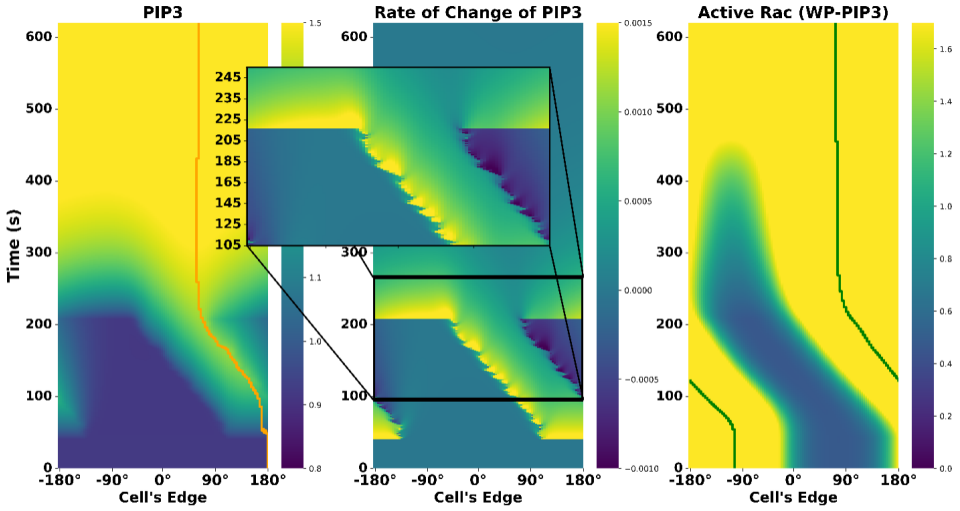

Figure A.1: Simulations of the WP model with PIP3 and inhibitor held constant, showing response for local-to-global stimulation. Left to right: kymographs of PIP3, its rate of change, and active Rac. Upon global stimulation, the Rac zone remains fixed in place until polarization is lost due to sustained stimulation.

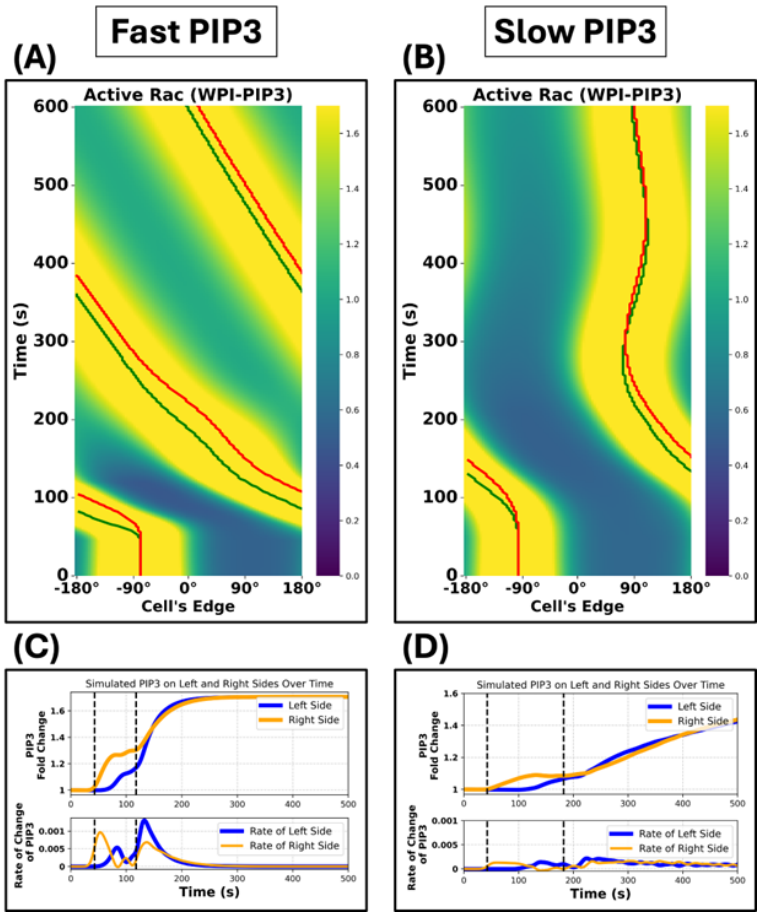

Figure A.2: Effect of PIP3 dynamics on Rac response. (Top) Kymographs of active Rac for fast (A) and slow (B) PIP3 dynamics, obtained by globally scaling the PIP3 equation with a timescale parameter. Green and red curves track the peaks of Rac and inhibitor, respectively. (Bottom) Time-dynamics of PIP3 (fold change, top graph) and its rate of change (bottom graph) on the left and right sides of the cell. Dashed vertical lines indicate the onset of local stimulation (first line) and the switch to global stimulation (second line). In the fast PIP3 case, PIP3 becomes uniform across the domain (equal levels on left and right side) before Rac can respond to any residual asymmetry, resulting in continued rotation. In the slow PIP3 case, the PIP3 peak persists too long, anchoring Rac and leading to oscillatory drift rather than full reversal. Only intermediate PIP3 dynamics (not shown) enable transient directional bias, producing successful reversal.

A.4 Fitting Parameters:

To accurately map my model simulations to real cellular dimensions, I first extracted the characteristic size of neutrophil-like HL-60 cells from the imaging data provided in [47]. The dataset in [47] includes a conversion factor from image pixel to physical units µm, which I used to quantify the perimeter, area, and Aspherity of the cells.

Geometric measure	Value ± Standard Deviation
Perimeter	76.0 ± 14.12 µm
Major Diameter	25.2 ± 3.88 µm
Minor Diameter	8.82 ± 2.26 µm
Area	222.2 ± 75.95 µm^2
Aspherity	1.46 ± 0.048

Table A.1: Geometric characteristics of motile HL-60 cells in the reversal experiment from Town & Weiner [47]. Values represent the mean ± standard deviation for perimeter, area, diameters and Aspherity.

To increase spatial fidelity, I tripled the resolution of the experimental pixel-to-µm ratio in my CPM simulations, and rescaled diffusion rates to preserve consistent dynamics.

A.4.1 Time-Dependent Reaction Parameters

To fit the temporal dynamics of Rac activity in latrunculin-treated cells, I used a least-squares minimization procedure to identify parameter sets that best reproduce the experimental Rac responses shown in Figure 2.2. These datasets track fold-changes in Rac activity over time following a double-pulse protocol: cells were stimulated globally for 180 seconds, followed by a rest phase (no stimulation) of 120 seconds, and then stimulated again for another 180 seconds. Because latrunculin inhibits F-actin polymerization and immobilizes the cells, spatial effects and feedback from shape change were absent, enabling me to simplify the model to its ODE form with only the reaction kinetics. In these experiments, light stimulation activates PI3K, leading to the production of PIP3, which in turn promotes Rac activity. The observed variability in PIP3 responses provided a range of inputs, enabling me to capture some of the heterogeneity in Rac dynamics across cells by fitting parameters to each individual cell.

For each cell j, I minimized the cost function

$$C_j = \sum_{i=1}^{N} \left(R_{ij}^{\text{exp}} - R_{ij}^{\text{sim}} \right)^2,$$

where R_{ij}^{exp} is the experimental fold-change of Rac in cell j at time point t_i, and R_{ij}^{sim} is the corresponding simulation prediction. Here, N denotes the number of interpolated time points ($N \approx 85{,}000$). Rac activity was normalized to a baseline value of 1 for each cell using its pre-stimulus level.

I used the Differential Evolution algorithm from the `scipy.optimize` package to perform the global optimization. DE is a stochastic population-based method that iteratively improves parameter estimates using mutation, crossover, and selection operations (Price, K et al., [40]). The DE optimizer was initialized using Latin Hypercube Sampling to ensure broad coverage of parameter space. Each ODE was solved using the `solve_ivp` function from the `scipy.integrate` package.

Before each simulation, the system was run to steady state to determine pre-stimulus levels, allowing me to create a baseline for computing fold change. To fit the double-pulse dataset, the PIP3 fold-change data were interpolated from experimental measurements and treated as a known time-dependent input to Rac. This allows me to isolate Rac and inhibitor dynamics from uncertainties in upstream signalling.

The parameters obtained through this fitting procedure are listed in Table 2.1. In total, I obtained 58 successful fits for the WP model and 87 for the WPI model. (The WP model is known to be rather sensitive). These fits produced parameter distributions from which I later sampled in order to preserve biological heterogeneity in my simulated cells.

A.4.2 AIC Model Comparison

To assess whether the WPI model provides a better fit than the WP model while accounting for its additional parameters, I computed the Akaike Information Criterion (AIC) for both models using their best-fit residuals and number of parameters. AIC score is defined as:

$$\text{AIC} = 2k + n \ln(\text{RSS}/n),$$

where k is the number of fitted parameters, n the number of data points, and RSS is the residual sum of squares.

I applied this calculation to the temporal fits from all double-pulse stimulation experiments. For this dataset, both models were evaluated using

the same 425 individual cells, using their PIP3 data directly as a known input function for $p(x,t)$ in the model. The WPI model had three additional parameters over the WP model, due to the inhibitor dynamics.

The resulting AIC values are shown in Table 2.2. The difference in ΔAIC was substantial, indicating strong evidence in favour of the WPI model.

A.4.3 Fitting Diffusion Parameters from Spatial Data

To estimate the relative rates of diffusion for active and inactive Rac, Rac-inhibitor, and PIP3, I simulated the full spatio-temporal WPI-PIP3 model. The reaction-diffusion equations were discretized in space using second-order central differences in a periodic 1D domain, with $M = 100$ grid points. This yields a tridiagonal Laplacian matrix with periodic boundary conditions. Time integration was carried out using the Crank-Nicolson method for diffusion terms and explicit Euler method for the reaction terms, implemented via operator splitting. Linear systems arising from the semi-implicit update steps were successfully solved using a sparse matrix routines from `scipy.sparse` and `scipy.sparse.linalg`.

The five stimulus protocols were: no stimulus (50 cells), front or side stimuli (45 and 15 cells, respectively), global (39 cells) and local-to-global switch (25 cells). For each condition, the fluorescence intensity around the cell edge was recorded over time. The spatial domain was represented from 0 to 2π with 100 evenly spaced grid points.

Because computing model predictions across all spatial and temporal points for each cell is computationally expensive, I used the average response for each protocol for fitting purposes. The model output was compared to this mean response using a least-squares objective function, and the Differential Evolution algorithm (as in the temporal fitting) was used to optimize the relative rates of diffusion.

To avoid nonphysical or biologically implausible parameter sets, I incorporated penalties into the cost function. For instance, solutions with slower diffusion for inactive Rac relative to active Rac were heavily penalized, based on the known binding of active Rac to the cell membrane. Other penalties were also explored, including a penalty for failure to reverse orientation in response to the local-to-global protocol.

A.4.4 Stimulus Normalization

When trying to fit the model to multiple stimulation protocols, I modified the input stimulus $S(x,t)$ to include a normalization factor, dividing it by

its integral over the cell edge.

$$S_{\text{new}}(x,t) = \frac{S(x,t)}{\int_\Omega S(x,t)} \tag{A.1}$$

This normalization reflects the limited range of signalling capacity that biological cells can sense. Mathematically, this normalization helps to balance the model's response to local versus global inputs. Without this adjustment, parameter sets would often fit one protocol well but fail another. Local-fitted models caused overstimulation under global input, leading to a spatial homogeneous solution, while global-fitted ones corresponded to very slow response to local cues. With the normalized stimulus, I achieved consistent fits and lower error across all protocols.

A.4.5 Results of Spatial Fitting

While Differential Evolution is a global optimization method, the complexity of the parameter space and model outputs in my system makes it unlikely that any single run finds a true global minimum. Moreover, parameter sets with the lowest squared error did not always yield the correct qualitative behaviours, such as proper reversal or sustained polarity. Slight changes in initialization often led to different final fits. For each fitting run, I logged the tested parameter sets, their associated errors, and key model behaviours (e.g., reversal success), allowing me to identify sets that balanced quantitative accuracy with expected biological responses. The parameter set I report here was selected for having near-minimal error while still preserving these key behaviours.

Fitting the WP model was particularly challenging. Even during the temporal fitting Table 2.1, several parameter sets failed to converge to biologically meaningful solutions, reflected in the lower success count (58 for WP vs. 87 for WPI). In the spatial setting, this issue persisted. Many WP fits converged to parameter sets that minimized error but led to implausible results, often producing nearly equal diffusion rates for active and inactive Rac. Penalties for missing reversal behaviour were not applied to WP, since it cannot reverse.

The final reported diffusion rates are in units of rad^2/s, representing effective diffusion along the 1D edge of the 2D projected cell shape. To approximate physical diffusion coefficients in $\mu\text{m}^2/\text{s}$, I used the mean perimeter of motile cells from the reversal experiment dataset (76 µm) to scale the values accordingly. Specifically, since the 1D domain has length 2π, the conversion factor is $(76/2\pi) \approx 146$, which I applied to all fitted values. A summary

table of the raw fitted values, their converted counterparts in µm^2/s, and the resulting diffusion rate ratios are given in Table A.2.

Diffusion Coefficient	Ratio (norm. to D_u)	rad^2/s	μm^2/s
D_u (Active Rac)	1.00	0.080	11.705
D_v (Inactive Rac)	6.40	0.510	74.617
D_h (Inhibitor)	0.47	0.037	5.413

Table A.2: Fitted diffusion coefficients for Rac model components. Values in µm^2/s are computed by rescaling from a $[0, 2\pi]$ domain to a perimeter of 76 µm. Note that this significantly overestimates the true diffusion, as explained below.

However, it is important to keep in mind that these values are "effective rates" of model diffusion along a 1D cell perimeter, based on a 2D fluorescence projection of a 3D phenomenon. The mapping to actual rates of diffusion depend on the geometry. To better understand how these fitted rates compare to real cellular diffusion, we (Leah Edelstein-Keshet and I) next consider how geometry and dimensionality affect diffusion scaling.

Scaling diffusion

In my simulations, the signalling components are restricted to the cell perimeter, whereas in the real cells, they diffuse on the membrane surface (active form) and in the cell bulk. Here we show how the "effective" rates of diffusion that we found in fitting my model to data in Table A.2 correspond to "real rates of diffusion" that would be measured in cells.

In a CPM simulation, the user specifies a target cell area A_0 (in pixels), and a target perimeter, P_0. As a first approximation, the mean diameter of a simulated cell is

$$d_0 \approx 2\sqrt{A_0/\pi}.$$

The perimeter can be expressed as

$$P_0 = \phi(\pi d_0) = \phi \cdot 2\sqrt{\pi A_0}$$

where $\phi > 0$ is the previously defined "Aspherity".

The ratio of the length of the cell perimeter (the domain of the model PDEs) to the cell diameter (1D slice of the domain where actual diffusion takes place) is

$$\frac{P_0}{d_0} = \phi\pi.$$

For my simulations, the Asphericity was set to $\phi = 1.4$ to obtain cells resembling neutrophils, so we have a domain ratio that corresponds to

$$\frac{L_1}{L_2} = \frac{P_0}{d_0} \approx 3.14 \cdot 1.4 \approx 4.4$$

It is well known that effective rates of diffusion in domains of size L_1, L_2 have the scaling property

$$\frac{D_1}{D_2} \approx \left(\frac{L_1}{L_2}\right)^2 \approx 20.$$

More detailed calculation that represents the 2D geometry of diffusion on the cell surface introduces Bessel functions. This mapping from 1D to 2D also affects the comparison (reducing the "real diffusion" by comparison to the model's "effective diffusion value" along the perimeter).

Hence, the values fitted for the model imply that actual rates of diffusion are roughly 10-20 fold lower, well in line with values of diffusion for GTPases cited in the literature. For example in [39], typical values are given as 0.1 μm^2 for diffusion of active GTPase (in the membrane) and 10 μm^2 for diffusion of the inactive GTPase (in the bulk).